Universidad Nacional Autónoma de México

Doctorado en Astrofísica
Instituto de Radioastronomía y Astrofísica

MASAS DINÁMICAS DE OBJETOS JÓVENES BINARIOS EN REGIONES DE FORMACIÓN ESTELAR CERCANAS

T E S I S

Para optar por el grado de
Doctora en Ciencias (Astrofisíca)

PRESENTA:
Norida Jazmín Ordóñez Toro

Tutores:
Dr. Sergio A. Dzib, Max Planck Institut für Radioastronomie
Dr. Laurent Loinard, Instituto de Radioastronomía y Astrofísica

Morelia, México, Marzo 2024

Dedicado a mi familia, especialmente a mis padres,
por su amor incondicional,
su infinito apoyo, esfuerzo y confianza,
y por creer siempre en mis sueños.

“A ese infinito cielo que danza con una sinfonía de luz y tiempo,
mientras los sueños acaban por tener alas.”

MASAS DINÁMICAS DE OBJETOS JÓVENES BINARIOS EN REGIONES DE FORMACIÓN ESTELAR CERCANAS

RESUMEN

Una fracción significativa de las estrellas que vemos en el cielo nocturno no están aisladas, sino que forman parte de sistemas estelares múltiples compuestos por dos o más componentes. De hecho, se estima que más de la mitad de las estrellas en nuestra galaxia se encuentran en sistemas binarios o múltiples, donde dos o más estrellas orbitan alrededor de su centro de masa común. Estos sistemas son fundamentales para realizar mediciones precisas de los parámetros físicos estelares, ya que permiten determinar de manera directa las masas estelares, un parámetro crucial que influye en la luminosidad, la temperatura, la evolución y el destino final de una estrella. La determinación precisa de las masas estelares, especialmente en las etapas tempranas de evolución, presenta desafíos significativos, ya que estos sistemas suelen estar embebidos en regiones densas de gas y polvo interestelar, lo que dificulta las observaciones en longitudes de onda como la óptica. Las observaciones en radiofrecuencias, como las realizadas con el *Very Long Baseline Array* (VLBA), permiten superar estas limitaciones al penetrar dichas regiones densas y obtener datos precisos sobre las propiedades dinámicas de estos sistemas. Gracias a estas observaciones, es posible calcular las masas dinámicas de las componentes individuales, un método basado en la interacción gravitacional entre los cuerpos que conforman el sistema. Esto contrasta con las estimaciones derivadas de métodos fotométricos, que dependen de la luminosidad y los modelos de evolución estelar. Por lo tanto, el estudio de las masas dinámicas en sistemas estelares jóvenes, tanto múltiples como binarios, permite probar y refinar los modelos evolutivos de estrellas en la pre-secuencia principal, contribuyendo así a una mejor

comprensión de la dinámica estelar y de las propiedades de sistemas estelares complejos.

En esta tesis, presentamos mediciones precisas de las masas dinámicas de sistemas estelares jóvenes, con un enfoque particular en sistemas compuestos por estrellas de masa intermedia. En este estudio, nos centramos en los sistemas S1 en Ofiuco y EC 95 en Serpens, presentando tres estudios que abordan distintos aspectos de cada fuente. Para lograrlo, utilizamos observaciones de alta resolución realizadas con el VLBA como parte del proyecto *Dynamical Masses of Young Stellar Multiple Systems with the VLBA* (DYNAMO - VLBA). Este proyecto está dedicado al estudio de sistemas cercanos binarios y múltiples de la pre-secuencia principal, caracterizados por emisiones de radio detectables y separaciones angulares típicas del orden de milisegundos de arco. Dado que misiones como Gaia no pueden resolver estos sistemas debido a sus pequeñas separaciones angulares, las observaciones con el VLBA son esenciales para determinar sus parámetros orbitales. En el caso del sistema S1, el miembro estelar más luminoso y masivo de la región de formación estelar de Ofiuco, encontramos que la componente primaria, S1A, tiene una masa de 4.115 ± 0.039 M$_\odot$, significativamente menor que el valor previamente reportado de ~ 6 M$_\odot$, basado en su tipo espectral. Esta discrepancia sugiere que los modelos utilizados para estimar la masa de S1A, basados en su posición en el diagrama de Hertzsprung-Russell podrían estar sobrestimando la masa en al menos un 25%. Por otro lado, la componente secundaria, S1B, tiene una masa de 0.814 ± 0.006 M$_\odot$, consistente con una estrella joven de baja masa, la cual detectamos por primera vez durante su paso por el periastro.

En el sistema triple EC 95 en Serpens, medimos las masas de EC 95A y EC 95B, obteniendo 2.15 ± 0.10 M$_\odot$ y 2.00 ± 0.12 M$_\odot$, respectivamente; en este caso, los modelos de evolución estelar concuerdan bien con estas masas dinámicas. Además, estimamos por primera vez la masa de la tercera componente, EC 95C, en $0.26\,^{+0.53}_{-0.46}$ M$_\odot$, con un período orbital de 172 ± 14 años.

Estas estimaciones de masas dinámicas, derivadas de datos del VLBA, no dependen de suposiciones sobre los parámetros físicos de las estrellas y resultan fundamentales para validar y ajustar los modelos teóricos de evolución estelar en pre-secuencia principal. Los resultados obtenidos no solo proporcionan restricciones valiosas para estos modelos, sino que también aportan nueva información sobre la dinámica y formación de sistemas estelares de masa

intermedia, contribuyendo así a una comprensión más profunda de la estructura y evolución estelar en regiones de formación estelar cercanas.

Palabras clave

Masas dinámicas, estrellas binarias, formación estelar, astrometría, Dinámica estelar.

DYNAMICAL MASSES OF YOUNG BINARY OBJECTS IN NEARBY STAR FORMING REGIONS

ABSTRACT

A significant fraction of the stars we see in the night sky are not isolated but are part of multiple stellar systems composed of two or more components. In fact, it has been estimated that more than half of the stars in our galaxy are found in binary or multiple systems, where two or more stars orbit around their common center of mass. These systems are fundamental for obtaining accurate measurements of stellar physical parameters, as they allow direct determination of stellar masses, a crucial parameter that influences the luminosity, temperature, evolution, and final fate of a star. Precise determination of stellar masses, especially in the early stages of evolution, presents significant challenges, as these systems are often embedded in dense regions of gas and interstellar dust, making observations in wavelengths such as the optical difficult. Radiofrequency observations, like those performed with the *Very Long Baseline Array* (VLBA), overcome these limitations by penetrating such dense regions and providing detailed data on the dynamical properties of these systems. Thanks to these observations, it is possible to calculate the dynamical masses of individual components, a method based on the gravitational interaction between the bodies that make up the system. This contrasts with estimations derived from photometric methods, which depend on luminosity and stellar evolution models. Therefore, studying dynamical masses in young multiple and binary systems enables testing and refining evolutionary models for pre-main sequence stars, thereby contributing to a better understanding of stellar dynamics and the properties of complex stellar systems.

In this thesis, we present precise measurements of the dynamical masses of young stellar systems, with a particular focus on systems composed of intermediate-mass stars. In this study, we focused on the S1 system in Ophiuchus and the EC 95 system in Serpens, presenting three studies that address different aspects of each source. To achieve this, we used high-resolution observations conducted with the VLBA as part of the *Dynamical Masses of Young Stellar Multiple Systems with the VLBA* (DYNAMO - VLBA) project. This project is dedicated to the study of close binary and multiple systems on the pre-main sequence, characterized by detectable radio emissions and typical angular separations on the order of milliarcseconds. Since missions like Gaia cannot resolve these systems due to their small angular separations, VLBA observations are essential to determine their orbital parameters.

In the case of the S1 system, the brightest and most massive stellar member of the Ophiuchus star-forming region, we found that the primary component, S1A, has a mass of $4.115 \pm 0.039\ M_\odot$, significantly lower than the previously reported value of $\sim 6\ M_\odot$ based on its spectral type. This discrepancy suggests that the models used to estimate the mass of S1A based on its position in the Hertzsprung-Russell diagram, might overestimate the mass by at least 25%. On the other hand, the secondary component, S1B, has a mass of $0.814 \pm 0.006\ M_\odot$, consistent with a young low-mass star, which we detected for the first time during its periastron passage.

In the triple system EC 95 in Serpens, we measured the masses of EC 95A and EC 95B, obtaining $2.15 \pm 0.10\ M_\odot$ and $2.00 \pm 0.12\ M_\odot$, respectively; in this case, stellar evolution models agree well with these measured dynamical masses. Additionally, we estimated for the first time the mass of the third component, EC 95C, as $0.26^{+0.53}_{-0.46}\ M_\odot$, with an orbital period of 172 ± 14 years.

These dynamical mass estimates, derived from VLBA data, do not rely on assumptions about the physical parameters of the stars and are fundamental for validating and refining theoretical models of stellar evolution in the pre-main sequence. The results not only provide valuable constraints for these models but also offer new insights into the dynamics and formation of intermediate-mass stellar systems, contributing to a more detailed understanding of the structure and evolution of stars in nearby star-forming regions.

Keywords

Dynamical masses, binary stars, stars:formations, astrometry, stars:kinematics

Acknowledgments

Agradezco profundamente a mis queridos padres, quienes han sido mi mayor fortaleza a lo largo de la vida. Su amor incondicional y su confianza infinita han iluminado cada paso en mi camino.
A mi pareja, Osbaldo, cuyo amor llegó como una cálida luz para abrigar mi alma. Gracias por caminar a mi lado, por tu apoyo constante y por ser mi fuente inagotable de inspiración.
A mis directores de tesis, el doctor Sergio A. Dzib y el doctor Laurent Loinard, les expreso mi más sincero agradecimiento.
Al doctor Sergio A. Dzib, por invitarme a formar parte de su proyecto y confiar en mí para llevarlo a cabo. Su orientación y generosidad han sido pilares fundamentales en este trabajo.
Al doctor Laurent Loinard, por su constante apoyo, guía y disposición a lo largo de mi doctorado, que fueron esenciales para superar los retos y alcanzar esta meta.
A ambos, les agradezco no solo como directores, sino también como personas. Su apoyo, tanto humano como profesional, ha dejado una huella invaluable en mi trayectoria y ha enriquecido profundamente esta experiencia.
Al Consejo Nacional de Ciencia y Tecnología (CONAHCyT) por otorgarme la beca que hizo posible la realización de mis estudios de doctorado. Agradezco también el apoyo financiero de los proyectos DGAPA PAPIIT IN108324 e IN112820, así como del CONACyT-CF grant 263356, los cuales fueron fundamentales para el desarrollo de esta investigación y facilitaron mi participación en congresos y escuelas académicas.
Finalmente, expreso mi más profundo agradecimiento al pueblo mexicano por acogerme en su maravilloso país. A mis amigos y a todas las personas que me acompañaron en este proceso, gracias por su apoyo incondicional, sus palabras de aliento y su sabiduría.

Publications

This thesis is a compilation of the following articles, which were derived directly from the work conducted by the author.

- ***Dynamical Mass of the Ophiuchus Intermediate-mass Stellar System S1 with DYNAMO-VLBA***
  Ordóñez-Toro, J., Dzib, S.A., Loinard, L., Ortiz-León, G., Kounkel, M.A., Masqué, J.M., Medina, S.-N.X., Galli, P.A.B., Dupuy, T.J., Rodríguez, L.F., Quiroga-Núñez, L.H., 2024, *The Astronomical Journal* (AJ), DOI:10.3847/1538-3881/ad1bd3.

- ***VLBA Detections in the Oph-S1 Binary System near Periastron: Confirmation of its Orbital Elements and Mass***
  Ordóñez-Toro, J., Dzib, S.A., Loinard, L., Ortiz-León, G., Kounkel, Galli, P.A.B., M.A., Masqué, J.M., Dupuy, T.J., 2024,
  (*Accepted, Monthly Notices of the Royal Astronomical Society* (MNRAS)), arXiv:2503.04594.

- ***Dynamical Mass of the Serpens Intermediate-mass Young Stellar System EC 95 with DYNAMO-VLBA***
  Ordóñez-Toro, J., Dzib, S.A., Loinard, L., Ortiz-León, G., Kounkel, M.A., Masqué, J.M., Medina, S.-N.X., Galli, P.A.B., Rodríguez, L.F., Quiroga-Núñez, L.H., 2024,
  (submitted to *Monthly Notices of the Royal Astronomical Society* (MNRAS)).

Publications not included in this thesis but produced as part of the doctoral research.

- ***Very Long Baseline Interferometry Detection of Nearby (<100 pc) Young Stars. Pilot Observations***
  Dzib, S.A., Loinard, L., Launhardt, R., **Ordóñez-Toro, J.**, 2024,
  Astronomy & Astrophysics (A&A), DOI: 10.1051/0004-6361/202243818.

- ***Accurate Proper Motions of the Protostellar Binary System L 1551 IRS 5***
  Hernández-Garnica, R., Loinard, L., Durán, A., **Ordóñez-Toro, J.**, et al., 2024,
  Monthly Notices of the Royal Astronomical Society (MNRAS), DOI: 10.1093/mnras/stae2482.

- ***Characterising the Multiple Protostellar System VLA 1623-2417 with JWST, ALMA, and VLA***
  Radley, I.C., Busquet, G., Ilee, J.D., Liu, H.B., Pineda, J.E., Pontoppidan, K.M., Macías, E., Maureira, M.J., Bianchi, E., Bourke, T.L., Codella, C., Forbrich, J., Girart, J.M., Hoare, M.G., Hernández-Garnica, R., Jiménez-Serra, I., Loinard, L., **Ordóñez-Toro, J.**, et al., 2025,
  American Astronomical Society Journal (AAS), accepted, Preprint, DOI: 10.48550/arXiv.2501.18348.

Contents

List of Figures

List of Tables

Chapter 1

Introduction

Many of the stars we see in the night sky are not solitary; rather, they are part of multiple stellar systems composed of two or more components. Observational studies indicate that the formation of multiple stellar systems is a natural consequence of the star formation process. These systems serve as excellent laboratories for studying stars because they form from the same gas and dust cloud and, therefore, share key physical properties such as age and metallicity. Currently, it is estimated that nearly half of the solar-type stars in our galaxy reside in binary or multiple systems, with this multiplicity fraction increasing with stellar mass (Duquennoy & Mayor, 1991; Raghavan et al., 2010; Duchêne & Kraus, 2013). Binary stars, consisting of two stars gravitationally bound to each other and orbiting a common center of mass, have been of particular interest in astronomical studies, and it is presumed that the term binary was first used by William Herschel in 1802 to describe double stars with mutual gravitational influence. Since then, interest in these systems has grown significantly, especially because they play essential roles across various fields of astrophysics, including stellar evolution and star formation.

Binary systems are crucial in astrophysics, as they provide the most direct method for measuring stellar masses by analyzing their orbital motion through Kepler laws and the equations of motion. Stellar mass is a fundamental parameter that governs nearly every aspect of a star lifecycle, shaping its internal structure, nuclear energy generation, evolutionary trajectory, and ultimate fate (Prialnik, 2009). Precise mass measurements from binary systems are essential for validating and refining theoretical models of stellar structure and evolution, particularly when derived from systems with accurately characterized orbits and components. Thus, the study of binary and multiple stellar systems is indispensable not only for understanding the mechanisms of star formation but also for establishing a robust foundation in stellar astrophysics.

In this chapter, we explore the key concepts and characteristics of the stellar objects involved in this thesis, focusing on young binary systems. Additionally, we provide a brief overview of the radio interferometry techniques used to obtain our data and introduce the concept of astrometry.

1.1 Multiple Stellar Systems Classification

Stable multiple systems exhibit a hierarchical structure. For example, in triple systems, a single star orbits a close binary pair, while in quadruple systems, two close binaries orbit one another. This hierarchical arrangement allows most multiple systems to be effectively described as binaries at several levels. Binary stars have been extensively studied and are typically categorized based on their detection methods and observable characteristics. The primary classifications include visual, astrometric, spectroscopic, and eclipsing binaries. Each type is briefly described below.

- **Visual Binaries**: These systems consist of stars that are spatially resolvable, allowing for separate observation of each component. As a result, their relative positions can be precisely measured, revealing changes over time as the stars orbit one another.

- **Astrometric Binaries**: In these systems, only one component is visible, but the binary nature is inferred through the oscillatory motion of the star on the sky. This variable proper motion indicates the presence of an unseen companion.

- **Spectroscopic Binaries**: In these systems, the presence of a companion is revealed through spectral analysis. The spectrum of the system may show two distinct sets of spectral lines or exhibit periodic Doppler shifts in the observed lines. These shifts, caused by the orbital motion of the star, indicate the gravitational influence of a companion.

- **Eclipsing Binaries**: In these systems, the orbital plane is nearly parallel to the observer's line of sight, allowing one star to periodically pass in front of the other, causing regular changes in observed brightness. The regular changes in luminosity are plotted over time to produce a light curve, which provides key information on the systems orbital and physical parameters.

The categories described are not mutually exclusive; for instance, a star may be classified as both a spectroscopic and an eclipsing binary, since these definitions often depend on the observational instrumentation used.

1.2 Formation Scenarios for Binary and Multiple Stellar Systems

The formation of binary and multiple stellar systems originates from distinct physical mechanisms operating within molecular clouds. The main scenarios that have been proposed (and which are not necessarily mutually exclusive) are turbulent fragmentation and disk fragmentation, each driven by specific environmental conditions and the initial physical properties of the clouds. These mechanisms contribute to the observed diversity in configurations of stellar systems, evident in variations in the relative orientation of the orbital planes and rotational axes of the stars, as well as in the orbital separations and evolutionary trajectories of their components.

The turbulent fragmentation theory suggests that turbulence within molecular clouds generates density fluctuations that lead to the formation of dense cores (Fisher, 2004; Goodwin et al., 2004; Padoan et al., 2007). Once gravity dominates these regions, they collapse to form stellar components. This process typically results in wide binaries with diverse configurations as each fragment evolves independently. Consequently, circumstellar disks and orbital planes in systems formed by turbulent fragmentation are often misaligned (Offner et al., 2010; Tobin et al., 2016; Lee et al., 2016). In Figure 1.1, the formation of a binary system via turbulent fragmentation is illustrated, showing the distribution of material density around the primary protostar.

The second mechanism, disk fragmentation, involves gravitational instabilities within massive

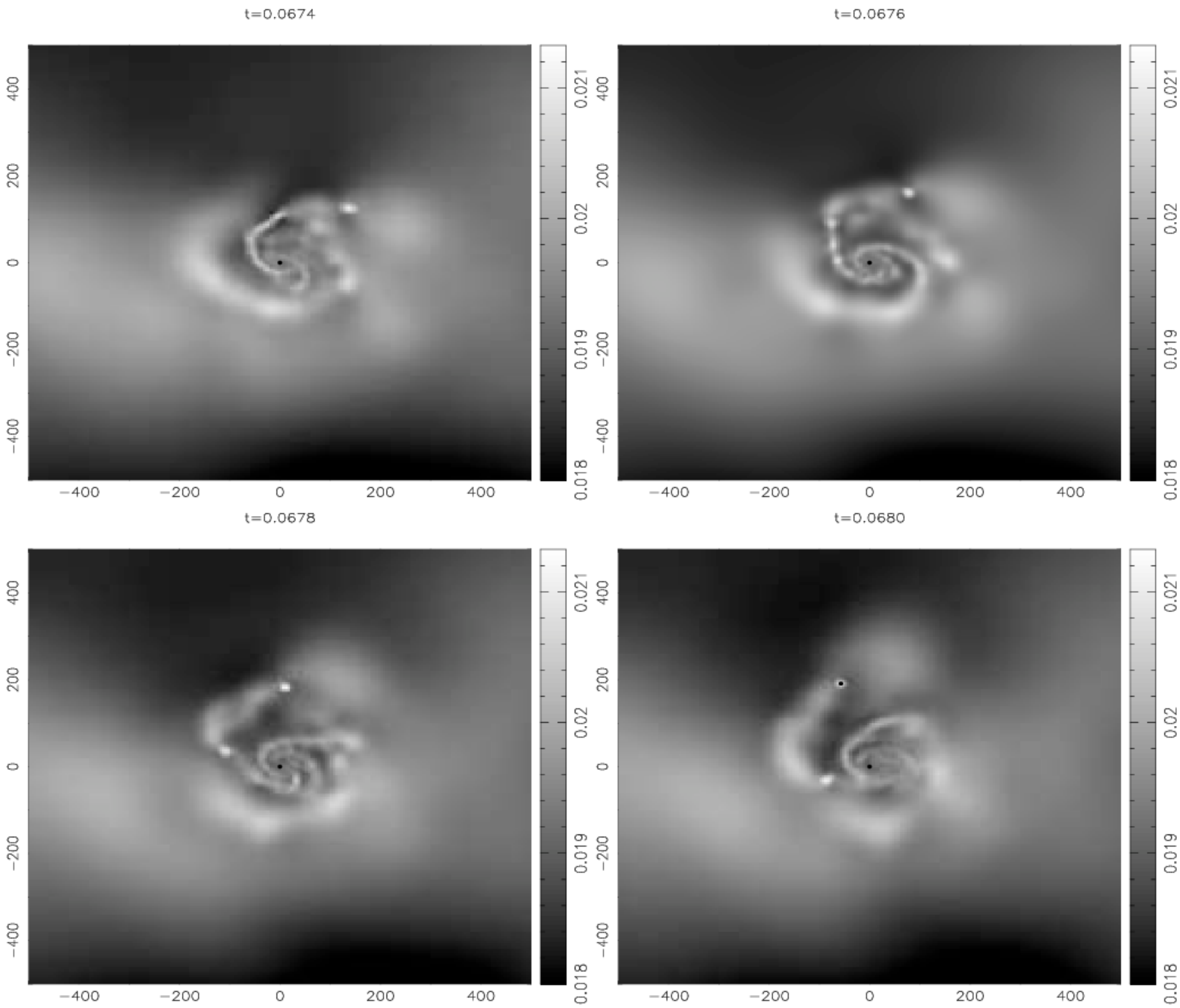

Figure 1.1: Simulation illustrating the formation of a binary system via turbulent fragmentation within a molecular cloud. The column-density plots show the evolution of the region around the primary protostar, highlighting how dense knots condense along spiral arms generated by turbulence. The spatial scale of the region is given in astronomical units (AU), and the grey-scale bar indicates the column density ($g\ cm^{-3}$). Image taken from Goodwin et al. (2004).

circumstellar disks surrounding protostars, leading to fragmentation (Adams et al., 1989; Bonnell & Bate, 1994; Stamatellos & Whitworth, 2009). In this process, large protostellar disks break into distinct clumps, forming compact stellar systems. These systems frequently exhibit close orbital separations (less than 500 AU) and are characterized by alignment among circumstellar disks, orbital planes, and rotational axes (Kratter et al., 2010; Tokovinin & Moe, 2020). Tokovinin & Moe (2020) further emphasizes that interactions with the circumbinary material, driven by differential accretion from the circumbinary disk, promote inward migration, leading to reduced orbital separations and the formation of very short-period binary systems. Additionally, these systems tend to have components with similar masses, although this trend decreases with the logarithm of the period (log P). While disk fragmentation typically produces components with comparable masses, short-period binary systems with significantly different mass components have also been reported (Prato et al., 2002; Morales-Calderón et al., 2012; Dudorov & Eretnova, 2016). In Figure 1.2, the fragmentation of a massive protostellar disk into multiple stellar components is illustrated.

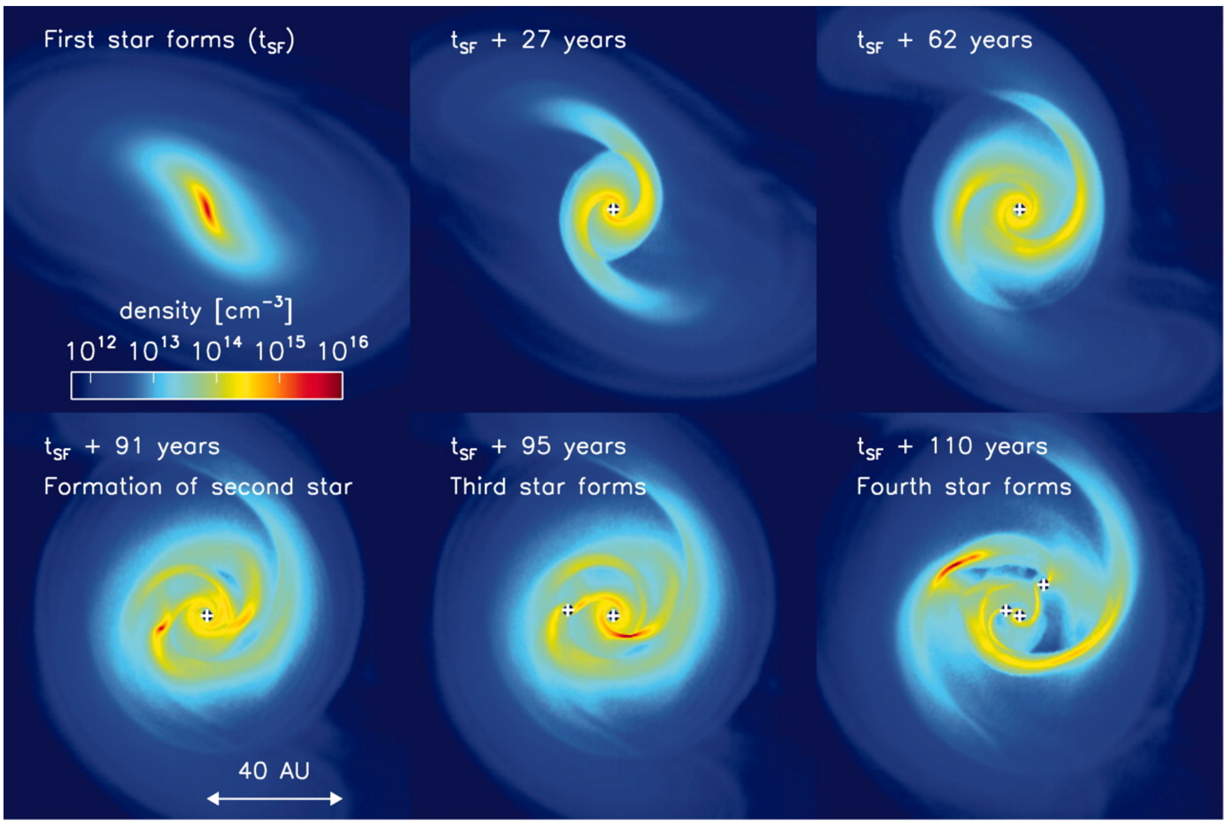

Figure 1.2: Simulation illustrating the formation, evolution, and fragmentation of a massive protostellar disk within a 120 AU region around a protostar, leading to the formation of multiple stellar components. Image taken from Clark et al. (2011).

Both mechanisms may act sequentially in star-forming regions. Turbulent fragmentation could initially produce multiple fragments, followed by disk fragmentation within some of these fragments, leading to complex hierarchical systems. In addition to these mechanisms, the rotation of the protostellar cloud can influence the multiplicity by affecting both fragmentation patterns and the orbital orientations of the resulting systems. Observational evidence supports turbulence as a dominant factor in forming wide companions, while rotation plays a secondary role in shaping system configurations. Magnetic fields are also thought to modulate system formation by limiting the size of the disk and reducing the number of fragments in a collapsing cloud (Price & Bate, 2007; Zhao & Li, 2013).

These formation scenarios underscore the critical role of young stellar objects (YSOs) as the building blocks of binary and multiple stellar systems. Whether through turbulence or disk fragmentation, these processes give rise to protostars and their associated circumstellar environments, which evolve through distinct phases before reaching the main sequence. Understanding the properties and dynamics of YSOs is therefore essential to unravel the processes underlying the formation and evolution of binary systems. The following section delves into the characteristics, classification, and early evolutionary stages of YSOs, emphasizing their significance in the broader context of star formation.

1.3 Young Stellar Objects

Young stellar objects (YSOs) are stars in the early stages of their development, evolving toward the main sequence in the Hertzsprung–Russell (HR) diagram. Once they reach the main sequence, they begin fusing hydrogen in their cores. The pre-main sequence evolution of YSOs is generally accepted in the astronomical community, although certain details remain incompletely understood. These objects are deeply embedded within molecular clouds, surrounded by gas and interstellar dust, which limits observations at optical wavelengths. For this reason, YSOs are often studied in the infrared, X-ray, and radio bands, which allows us to peer through the surrounding material.

The classification of YSOs into distinct evolutionary stages was first introduced by Lada (1987) and Adams et al. (1987), who classified them into Classes I, II, and III based on the slope of their spectral energy distribution (SED) in the infrared, described by the spectral index α. The spectral index can be defined as a function of wavelength, $\alpha_\lambda = d\log(\lambda F_\lambda)/d\log\lambda$, where F_λ is the flux density per unit wavelength (between 2.2 and 25 μm) (Lada, 1987), or as a function of frequency, $\alpha_\nu = d\log(\nu F_\nu)/d\log\nu$, where F_ν is the flux density per unit frequency (Adams et al., 1987). This classification reflects the relative contributions of the central star and its circumstellar material, linking the observational properties to the evolutionary stage of the star. Later, André et al. (1993) added a Class 0 to describe the youngest and most deeply embedded objects, which emit primarily in the far-infrared and at submillimeter wavelengths (> 50 μm). These classifications outline the progression of young stars from their initial formation (Class 0) to the later stages of pre-main sequence evolution (Class III). A summary of this classification is presented in Figure 1.3.

During the early stages of stellar evolution, a star gains most of its mass by accreting gas and dust from its surroundings. Fragments of a molecular cloud or material from a circumstellar disk collapse under the influence of gravity, forming what is known as a *protostar*. This process generates increased pressure in the interior of the object, leading to higher temperatures (Shu et al., 1987). Initially, the protostar remains deeply embedded within a dense molecular cloud, and its spectral energy distribution exhibits strong emission in the far-infrared and submillimeter bands. This emission, associated with the surrounding gas and dust (at temperatures around 30 K), characterizes Class 0 YSOs (Feigelson & Montmerle, 1999; André et al., 1993). At this stage, the protostar is opaque at optical wavelengths since the surrounding material prevents radiation from escaping. As the protostar continues to collapse, part of the accreting material is funneled toward the center, while the rest is expelled into the interstellar medium via protostellar jets and bipolar molecular outflows. These jets play a crucial role in the early stages of star formation by removing excess angular momentum, which allows material in the circumstellar disk to continue accreting onto the protostar.

In the next evolutionary stage, the protostar continues to grow by accreting material from its surroundings. As a result of rotational effects, the surrounding cloud forms a disk, altering the paths of infalling material. These objects are classified as Class I YSOs, where the gas and dust envelope is less dense than in Class 0 objects. The spectral energy distribution, characterized by $\alpha_\lambda > 0$, shows a pronounced infrared excess, primarily originating from the dust envelope, although a significant portion of the emission comes from hotter material close to the protostar

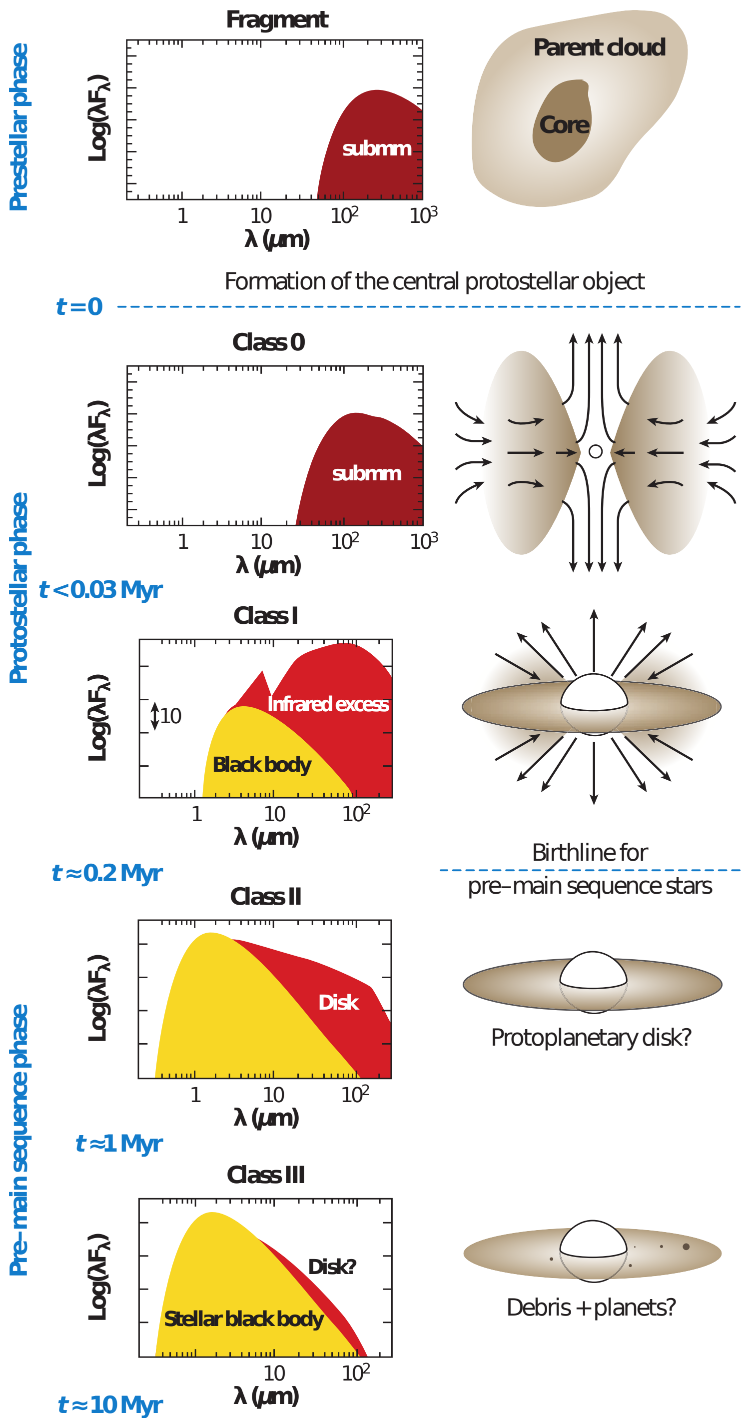

Figure 1.3: Representative diagram of the evolutionary stages of young stellar objects. The left column shows the spectral energy distribution, and the right column provides a system diagram for each stage. Image taken from Dauphas & Chaussidon (2011).

(André et al., 1993). The bipolar outflows interact with the interstellar medium, producing strong shock waves that heat and ionize the surrounding gas, giving rise to Herbig-Haro objects, which are key tracers of star formation activity (Dopita et al., 1982; Feigelson & Montmerle, 1999). During this phase, the protostar is surrounded by an accretion disk, where accretion occurs both from the envelope to the disk and from the disk to the central protostellar system (Eisner et al., 2005). This disk, often referred to as a protoplanetary disk, where planetary systems are presumed to form (Lada, 1991; Brogan et al., 2015). However, observational evidence suggests that circumstellar disks may begin to form as early as Class 0 (Zapata et al., 2013).

As the protostar evolves, accretion from the envelope to the disk decreases significantly, leading to the dissipation of the envelope (Fiorellino et al., 2021). This marks the transition to the pre-main sequence phase, where the object is classified as a Class II YSO and can be observed at optical wavelengths. The SED during this stage, characterized by $-1.5 < \alpha_\lambda < 0$, resembles that of a blackbody with a significant infrared excess caused by the heated material in the protoplanetary disk. This stage includes Classical T Tauri stars (CTTs), which are low-mass, variable stars (with masses < 2 $M_\odot$) of spectral types F, G, K, and M. CTTs are characterized by active accretion from their circumstellar disks, which leads to strong emission lines in their spectra, including prominent Hα emission indicative of ongoing accretion (Feigelson & Montmerle, 1999). Also present are Herbig Ae/Be (HAeBe) stars, the intermediate-mass counterparts to T Tauri stars, have masses typically ranging from 2–8 $M_\odot$ and exhibit spectral types A and B (Herbig, 1960; Lada & Wilking, 1984; Shu et al., 1987; Feigelson & Montmerle, 1999). These stars, precursors to main-sequence A and B stars, are characterized by prominent emission-line spectra, including strong Hα emission indicative of ongoing or residual accretion and the presence of circumstellar material (Manoj et al., 2006). Unlike CTTs, their disks tend to be more massive. Although Herbig Ae/Be stars are not expected to exhibit strong magnetic fields, observations have revealed organized magnetic fields, evident in variability and the alignment of jets or outflows (Hubrig et al., 2004, 2015; Wade et al., 2005; Alecian et al., 2013). This raises important questions about how such fields are generated and sustained in intermediate-mass stars, which are discussed in more detail in the following Section §1.3.1.

During the transition from Class II to Class III, the circumstellar disk gradually dissipates, marking the final pre-main sequence phase. The star has accreted or expelled nearly all its circumstellar material, leaving behind a very thin disk or only a debris disk. These objects are classified as Class III YSOs and are close to joining the main sequence. Their SED, characterized by $\alpha_\lambda < -1.5$, closely resembles a blackbody, as the majority of their emission comes from the central object. Class III YSOs include weak-lined T Tauri stars (WTTs; <2 $M_\odot$), which are characterized by faint or nearly absent circumstellar disks. Consequently, their infrared excess is minimal or nonexistent. They also exhibit significantly weaker emission lines in their spectra, including a much lower Hα equivalent width, indicating a drastic reduction in accretion activity compared to CTTs (Feigelson & Montmerle, 1999).

1.3.1 Nature of Radio Emission from YSOs

YSOs emit electromagnetic radiation across a wide range of wavelengths. Radio observations are particularly valuable for studying these objects, as they provide insights into their circumstellar environments, including ionized winds, jets, accretion activity, and magnetic fields. The radio emission from YSOs originates from both thermal and non-thermal mechanisms, which dominate at different evolutionary stages.

Thermal *free-free* emission is a mechanism observed primarily in the early stages of YSO evolution, particularly in Class 0 and Class I objects. This emission arises from the interaction of free electrons with ions in ionized gas, producing continuum radiation. It is often associated with partially ionized jets and outflows driven by accretion processes (e.g., Rodriguez, 1997).

As YSOs evolve into Class II and their circumstellar environments dissipate, non-thermal radiation becomes increasingly significant. A key mechanism of this emission is *gyrosynchrotron* radiation, produced by mildly relativistic electrons spiraling along magnetic field lines, typically as a result of magnetic reconnection events in the stellar magnetosphere (Güdel, 2002). This type of emission is characterized by high brightness temperatures, strong circular polarization, and variability on timescales of hours to days (Dulk, 1985; Hayashi et al., 1997). Gyrosynchrotron radiation is commonly observed during the pre-main sequence phase.

The mechanisms driving radio emission in YSOs are closely linked to their internal structure and energy transport processes. For low-mass stars (0.5–2 $M_{\odot}$), evolution follows the Hayashi track in the Hertzsprung-Russell diagram, where convection is the primary energy transport mechanism. The movement of ionized material in these stars, combined with differential rotation, generates strong surface magnetic fields (~1 kG) through the dynamo mechanism, creating the conditions for non-thermal emission (Parker, 1955).

For intermediate-mass stars (2–8 $M_{\odot}$), evolution follows the Henyey track in the Hertzsprung-Russell diagram, where radiative energy transport dominates. Although these stars are generally not expected to exhibit strong magnetic activity, a small fraction shows evidence of significant magnetic fields (Stelzer et al., 2005, 2006; Wade et al., 2011; Hubrig et al., 2009). Several hypotheses have been proposed to explain this phenomenon; one possibility is the presence of an invisible low-mass secondary component, which could generate magnetic activity (Stelzer et al., 2005, 2006). Another theory suggests that strong collisions of stellar winds could produce the non-thermal radiation detected (Skinner & Yamauchi, 1996). Additionally, temporary convective layers on the stellar surface, possibly driven by substellar deuterium burning or rapid differential rotation, have been proposed as mechanisms for generating magnetic fields in these stars (Palla & Stahler, 1993; Tout & Pringle, 1995; Skinner et al., 2004). One of the most accepted ideas nowadays is that the magnetic fields have a fossil origin (Schleicher et al., 2023). This means that the magnetic fields are remnants of the original magnetic field of the interstellar medium or were formed very early in the life of the star, and they have been preserved over time.

Massive stars (>8 $M_{\odot}$) transition rapidly through their early evolutionary stages without passing through a pre-main sequence phase. Their radio emission primarily arises from ionized stellar winds or optically thin compact HII regions, reflecting strong mass-loss rates and dynamic interactions within their ionized environments (Hughes, 1988; Estalella et al., 1991; Felli et al., 1998).

Radio observations provide a crucial perspective on the physics of YSOs, allowing us to penetrate the dense material in which they are embedded. The high resolution and sensitivity of modern instruments, particularly *radio interferometers*, have revolutionized the study of these objects, enabling detailed investigations of their emission mechanisms and circumstellar environments. This makes radio interferometry an indispensable tool for uncovering the processes governing star formation, as explored in Chapter 2.

1.4 The Importance of Nearby Star-Forming Regions

Understanding the formation and evolution of binary and multiple stellar systems requires observations in regions where stars are actively forming. Nearby star-forming regions, such as Ophiuchus, Orion, Serpens, Taurus, Upper Scorpius, among others, are particularly valuable for this purpose. Their proximity allows for detailed, high resolution observations of YSOs across multiple wavelengths, providing critical insights into the physical processes that drive star formation. These regions contain diverse populations of YSOs at various evolutionary stages, making them excellent natural laboratories for studying the properties and dynamics of young binary systems. In this thesis, we focus on Ophiuchus and Serpens due to their accessibility, rich stellar populations, and the unique opportunities to advance our understanding of young binary systems.

The Ophiuchus molecular cloud complex, situated at a distance of 137.3±1.2 pc (Ortiz-León et al., 2017b), is one of the nearest and most extensively studied regions of active star formation. This region has played a crucial role in our overall understanding of the processes involved in stellar formation (Wilking et al., 2008). The majority of the star formation occurs in the dense core known as Lynds 1688 (L1688), which hosts a cluster of YSOs with an average age of approximately 10^5 years (Wilking et al., 2008).

The most luminous and massive member of L1688, and of the entire Ophiuchus region, is the young Herbig Be star Oph S1 (also known as S1). Early radio observations revealed that S1 exhibits two primary components of radio emission: a thermal, extended region of about 20″ associated with a compact H II region, and a non-thermal, compact source embedded within this region (Andre et al., 1988). Subsequent VLBI observations identified the non-thermal component as originating from the magnetically active star S1. Notably, this system became the first young stellar object to be directly detected using VLBI techniques (Andre et al., 1991), making it a significant target for astrometric and dynamical studies. Figure 1.4 shows the ρ Ophiuchi cloud complex, with the bright star S1 prominently carving a glowing cavity in the surrounding gas, visible in the lower half of the image.

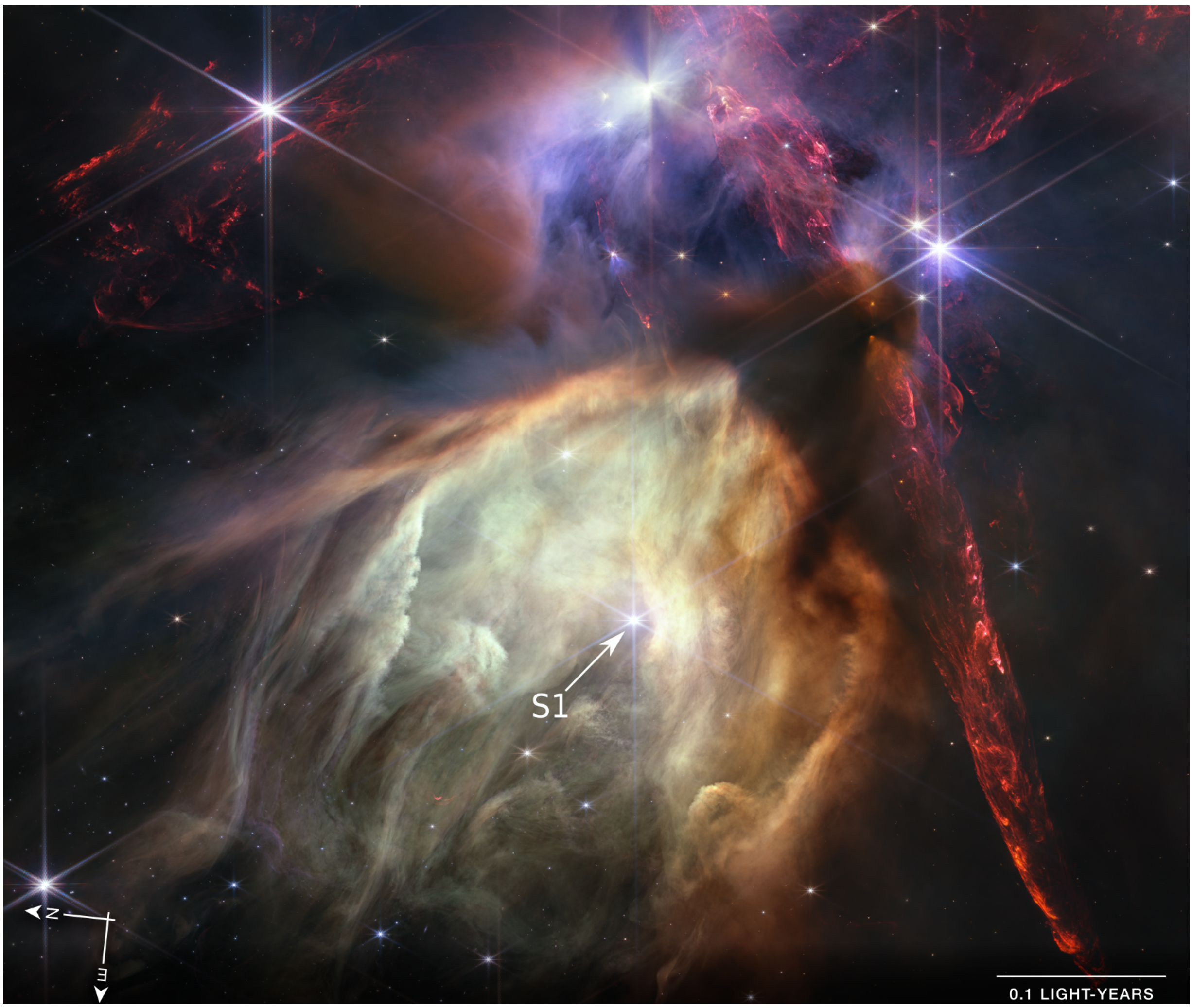

Figure 1.4: The ρ Ophiuchi cloud complex, imaged by NASA James Webb Space Telescope, highlights the bright star S1 in the lower half of the image. S1 carves a glowing cavity in the surrounding gas with its stellar winds. Credits: NASA, ESA, CSA, STScI, Klaus Pontoppidan (STScI), Image Processing: Alyssa Pagan (STScI).

The Serpens Molecular Cloud, located at a distance of 436.0 ± 9.2 pc (Ortiz-León et al., 2018b), is a prominent site of active star formation within the Aquila Rift complex. Distinguished by its rich population of YSOs, it has one of the highest fractions of Class 0/I objects among nearby star-forming regions (Eiroa et al., 2008; Dunham et al., 2015). This high proportion of very young protostars indicates ongoing star formation, making Serpens an exceptional laboratory for studying the earliest stages of stellar evolution.

The core region of the Serpens Molecular Cloud, often referred to as Serpens Main, contains several compact subclusters characterized by high stellar densities. Notable among these are the SVS 4 and SVS 2 groups (Kaas et al., 2004; Winston et al., 2007). In particular, SVS 4, is an infrared cluster embedded deep within the Serpens core and stands out as one of the densest young stellar sub-clusters known, with a stellar mass density of approximately 10^5 $M_\odot$ pc^{-3} (Eiroa & Casali, 1989). Recent observations using the Atacama Large Millimeter/submillimeter Array (ALMA) and the James Webb Space Telescope (JWST) have revealed complex filamentary structures, molecular outflows, and a remarkable alignment of protostellar jets, highlighting ongoing accretion and feedback processes shaping the region (Tychoniec et al., 2018; Green et al., 2024). Figure 1.5 shows the Serpens Nebula, highlighting the protostellar outflows (upper left), the characteristic region known as the Bat Shadow (center), and the dense regions blocking near-infrared light.

A particularly interesting system within the SVS 4 cluster is EC 95 (also known as [EC92]95). Early estimates of its spectral type (approximately a K2 star), age ($\sim 10^5$ years), and mass ($\sim$4 $M_\odot$) suggested that the source is a proto-Herbig Ae/Be star (Preibisch, 1999). Eiroa et al. (2005) suggested a Class II classification for this system, supported by observations of a modest mid-infrared excess (Preibisch, 1999; Haisch et al., 2002; Pontoppidan et al., 2004), weak veiling, and attenuated CO overtone rovibrational absorption lines (Doppmann et al., 2005). However, its flat-spectrum characteristics have also led to its classification as a Class 0/I object (Harvey et al., 2007; Winston et al., 2007). High-resolution interferometric observations revealed that EC 95 is a young multiple stellar system formed by two close components first observed by Dzib et al. (2010). More recently, Ortiz-León et al. (2017a) showed that EC 95 is a hierarchical triple system, making it an excellent target for investigating the formation mechanisms of multiple stellar systems and for testing theoretical models of early stellar evolution for intermediate-mass stars.

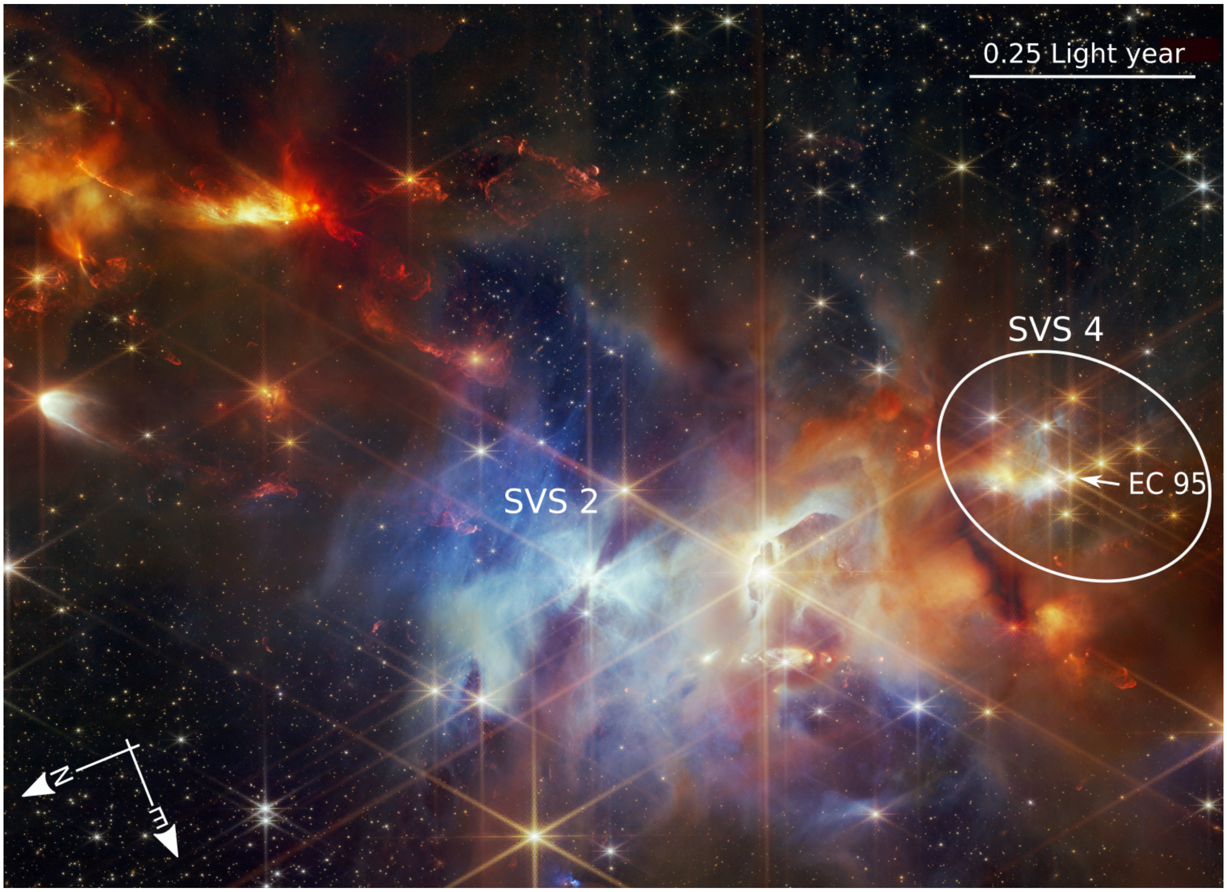

Figure 1.5: The Serpens Nebula, imaged by the Near-Infrared Camera (NIRCam: F140M - blue, F210M - green, F360M - orange, F480M - red), NASA James Webb Space Telescope, showcases aligned protostellar outflows (upper left, red streaks), the Bat Shadow at the center, and dense dark regions blocking near-infrared light. Credits: NASA, ESA, CSA, STScI, Klaus Pontoppidan (NASA-JPL), Joel Green (STScI).

1.5 Pre-main Sequence Stellar Evolution Models

Dynamical masses obtained from binary systems are essential for constraining stellar evolution models. This is particularly important for young stars, as pre-main sequence (PMS) evolution models are less reliable and less developed than their main sequence counterparts (e.g., Hillenbrand & White, 2004; Stassun et al., 2014). Models for young intermediate-mass stars are especially uncertain due to the scarcity of observational constraints. PMS models allow us to estimate fundamental stellar parameters, such as masses and ages, from observable quantities like luminosities and effective temperatures. Therefore, comparing the observational properties with the predictions of theoretical models using dynamically determined masses is highly valuable.

All PMS models use equations of state (EOS) to describe the relationship between pressure, temperature, and density in stellar material. The EOS provides the necessary thermodynamic properties for modeling stellar interiors. Additionally, opacities, which represent the ability of material to absorb or scatter radiation, are crucial for modeling energy transport within stars.

The *Opacity Project at Livermore* (OPAL) opacities are among the most widely used Rosseland mean opacities today. OPAL, a project from Lawrence Livermore National Laboratory, calculates precise opacities for stellar material under conditions of high temperature and density (Iglesias & Rogers, 1996). OPAL provides opacity tables for a wide range of temperatures and densities, helping to model the movement of energy from the core of the star to its surface. These opacities are crucial in determining whether energy can escape easily or becomes trapped, thus affecting the structure and evolution of the star. At lower temperatures, opacities from Ferguson et al. (2005) or Alexander & Ferguson (1994) are often employed, which include absorption by molecules and dust grains. Electron conduction opacities, important in dense regions, are generally taken from Potekhin (1999) or Cassisi et al. (2007), depending on the model. PMS models also consider nuclear reaction rates that generate the necessary energy during the contraction phase. These rates are primarily taken from the *Nuclear Astrophysics Compilation of Reaction Rates* (NACRE), which is an exhaustive collection of nuclear reaction rates relevant to stellar astrophysics (Angulo et al., 1999). NACRE provides evaluated and standardized data, focusing especially on deuterium burning, which plays a fundamental role during the early stages of PMS evolution. Convection is modeled using the *Mixing Length Theory* (MLT), with a parameter controlling the efficiency of convective energy transport. Additionally, some models include convective overshooting, which accounts for the penetration of convective motions beyond the boundaries set by the Schwarzschild criterion, where the energy transport transitions from convection to radiation. Furthermore, all PMS models rely on solving a set of stellar structure equations, which include:

- **Hydrostatic equilibrium**: Represents the balance between gravitational forces pulling the stellar material inward and pressure forces pushing outward. This condition ensures the stability of the star, maintaining its shape and preventing collapse or uncontrolled expansion.

- **Mass conservation**: Describes the relationship between the density and volume of stellar layers, explaining how the total mass contained within a certain radius is determined by summing the contribution of each spherical layer. In each layer, the differential mass is obtained by multiplying the local density by the differential volume of that layer; by integrating these contributions from the core to that radius, the accumulated mass in that sphere is obtained, which allows us to describe how mass is distributed within the stellar structure.

- **Energy transport**: Refers to the mechanisms by which energy is transferred from the core to the surface of the star. This process can occur through radiative transfer, where energy is carried by photons, or through convection, where energy is transported by the bulk motion of stellar material. The dominant mechanism depends on the local temperature gradient and opacity.

- **Energy generation**: Governs the production of energy through nuclear fusion reactions occurring in the star's core. These reactions convert lighter elements into heavier ones, releasing energy that counterbalances gravitational contraction and drives the star's luminosity.

Although all models share general features, each focuses on specific physical processes depending on the mass and evolutionary stage of a star. Below are the most commonly used models for studying intermediate-mass pre-main sequence stars:

- **Pre-main sequence Isochrones from Stellar Evolution (PISA)**: Focused on low- and intermediate-mass stars (0.2 to 7.0 $M_\odot$), these models include deuterium burning and use the OPAL EOS with low-temperature opacities (Tognelli et al., 2011).

- **Yonsei-Yale Stellar Models (Y^2)**: Designed for stars from 0.4 to 5.0 $M_\odot$, these models include helium and heavy-element diffusion and convective overshooting for stars above 1.2 $M_\odot$ (Yi et al., 2001).

- **Palla & Stahler Models**: These models consider accretion and accretion luminosity during star formation, covering masses from 0.1 to 6.0 $M_\odot$ (Palla & Stahler, 1999).
- **Padova and Trieste Stellar Evolution Code (PARSEC)**: Applicable to stars from 0.1 to 350 $M_\odot$, these models include mass loss, rotation, and mass-dependent convective overshooting (Nguyen et al., 2022).
- **Yale-Potsdam Stellar Isochrones (YaPSI)**: Focused on stars between 0.15 and 5.0 $M_\odot$, these models include magnetic inhibition of convection and starspots, relevant for young stars with strong magnetic activity (Spada et al., 2017).
- **Siess Models**: Covering stars from 0.1 to 7.0 $M_\odot$, these models include deuterium burning and consider the effects of metallicity on PMS evolution (Siess et al., 2000).
- **Bag of Stellar Tracks and Isochrones (BaSTI)**: Provide tracks for stars across a wide mass range, incorporating element diffusion, mass loss, and convective overshooting (Pietrinferni et al., 2004, 2006).
- **MESA Isochrones and Stellar Tracks (MIST-MESA)**: Built with the *Modules for Experiments in Stellar Astrophysics* code (MESA), these models cover a wide mass range and include rotation, mass loss, updated nuclear rates, and opacity tables (Paxton et al., 2011; Choi et al., 2016).

1.6 Objectives and Structure of this Thesis

The main goal of this thesis is to calculate the dynamical masses of the intermediate-mass young binary and multiple stellar systems S1 and EC 95, located in the star-forming regions of Ophiuchus and Serpens, respectively. High-resolution VLBA observations are used to determine the individual component masses, offering a unique opportunity to test pre-main sequence stellar evolution models. These observations are primarily part of the *Dynamical Masses of Young*

Stellar Multiple Systems with the VLBA (DYNAMO-VLBA) project.

In the opening Chapter 1, the concepts of star formation and the evolution of pre-main sequence stars were introduced, with a particular focus on binary and multiple systems. Chapter 2 presents the methodology for the analysis developed in this work, describing the theoretical principles required for the observations, the data calibration processes, and the fitting procedures used to determine astrometric and orbital parameters, as well as to calculate dynamical masses. Chapter 3 details the dynamical masses of the components in the Oph-S1 system, the most massive member of the Ophiuchus region, is presented, including orbital and astrometric parameters of S1A and S1B derived from high-resolution, multi-epoch VLBA data. Chapter 4 describes recent VLBA observations of S1 conducted near its periastron passage, which improve the orbital solution for S1A and S1B. In Chapter 5, the focus is on the multiple stellar system EC 95 in the Serpens star-forming region, presenting the dynamical mass measurements of the primary components, EC 95A and EC 95B, along with an analysis of the nature and mass of the third component, EC 95C. Finally, in Chapter 6, the main conclusions of this thesis are summarized, highlighting its contributions to the understanding of binary and multiple stellar systems.

Chapter 2

Methodology

This chapter describes the methodology employed in this thesis, which forms the basis for the analysis and results presented. It begins with a general overview of radio interferometry, highlighting its importance for studying the astrometry of multiple and binary young stellar objects (YSOs) with unprecedented precision. Next, the observations and data calibration process are described, detailing the steps taken to ensure accurate measurements. Using the calibrated data, the chapter delves into the analysis of orbital dynamics and astrometric fitting, explaining the methods used to derive astrometric and orbital parameters, which allow the determination of individual stellar masses in these systems. Finally, the chapter presents the analysis of the SED as a complementary approach to further constrain the physical properties of the studied systems.

2.1 Radio Interferometry and High-Precision Astrometry

In modern astronomy, radio interferometry has become an indispensable tool for studying young stellar objects (YSOs). This technique enables astronomers to peer through the dense material surrounding these stars, revealing crucial insights into their physical properties and environments. Among its many applications, radio interferometry excels at performing astrometry, which involves the precise measurement of celestial positions and motions. These high-precision measurements are essential for determining fundamental stellar parameters, including distance, mass, and luminosity. Such parameters provide critical information for understanding the physical processes driving star formation and the early evolution of stellar systems. One of the most direct and reliable methods for estimating the distances to YSOs is the determination of their trigonometric parallax. This technique leverages the apparent shift in the position of a star as observed from the orbit of Earth around the Sun. The parallax angle, denoted as π, is inversely related to the distance, d, and is calculated using the simple relationship $d = 1/\pi$, where π is measured in arcseconds and d in parsecs; this relation remains valid for relative parallax uncertainties below approximately 20%, whereas larger uncertainties suggest a Bayesian approach (Bailer-Jones, 2015). By combining the exceptional resolution of radio interferometry with this geometric approach, astronomers can accurately map the spatial distribution of YSOs and derive their intrinsic properties with unprecedented precision.

Accurate parallax measurements are essential for minimizing uncertainties in distance estimates. For YSOs, such precision directly improves the determination of stellar masses and luminosities, which are crucial for constraining theoretical models of star formation and evolution. Astrometry is particularly valuable for studying binary systems, which are common among YSOs. By observing the orbital motion of the binary components, it is possible to obtain direct mass measurements, providing robust benchmarks for stellar evolution models. Achieving such precise observations, however, requires instruments and techniques capable of addressing the challenges posed by dense environments and extremely small angular separations. While astrometric missions such as Gaia are highly effective for providing stellar parameters for many systems, they are not suited for resolving tight binaries. In nearby star-forming regions (distances < 500 pc), young binary systems often exhibit angular separations on the order of 0.01 arcseconds or smaller, with orbital periods ranging from one to a few decades. Additionally, if the Gaia astrometric solution is based on the assumption that each source is a single star, then for binary systems the derived parameters, such as parallax and proper motion, may be less reliable. In such cases, the RUWE (Renormalised Unit Weight Error), which evaluates the quality of the astrometric model fit, is used; RUWE values greater than 1.4 indicate that the single-star model does not properly fit the astrometric data (Lindegren et al., 2018). Observing such systems demands instruments with extremely high angular resolution and astrometric accuracy, making radio interferometric techniques indispensable. Among these, the *Very Long Baseline Interferometry* (VLBI) technique stands out as one of the most effective tools for achieving the required precision.

VLBI is a powerful technique in radio astronomy that links widely separated radio telescopes to achieve exceptional angular resolution. Each radio telescope operates independently, recording signals with extremely precise timestamps provided by atomic clocks. These signals are then combined at a central correlator, a system that processes and analyzes the data from multiple radio telescopes to compute the *visibility function*. This function encodes the amplitude and phase of the electromagnetic waves received by the antennas, capturing how each one observes the same object from different locations. The information contained in the visibility function is used in a process called *aperture synthesis*, which combines the data to reconstruct highly detailed images of the sky with a resolution equivalent to a single radio telescope as large as the maximum separation between the antennas (Thompson et al., 2001). The resolution achieved by VLBI is inversely proportional to the maximum baseline length, allowing spatial resolutions as fine as 1 milliarcsecond or better. This is described by the formula: $\theta = \lambda / B_{\max}$, where λ is the observed wavelength, and $B_{\max}$ is the maximum baseline length.
A key advantage of VLBI is its contribution to the definition and implementation of the *International Celestial Reference Frame* (ICRF), the fundamental reference system for astrometric observations, recognized by the *International Astronomical Union* (IAU). The ICRF is based on the positions of distant quasars, which appear as fixed points on the celestial sphere due to their immense distances. Its precision and stability have been enhanced over time by incorporating increasingly denser samples of quasars (Ma et al., 1998; Fey et al., 2015; Charlot et al., 2020). This anchoring enables VLBI to measure absolute proper motions and determine the position of a stellar system center of mass, which in turn facilitates the precise determination of individual orbital parameters and the calculation of the dynamical masses of components in binary systems.

One of the most advanced radio interferometers implementing this technique is the *Very Long Baseline Array* (VLBA). The VLBA consists of 10 radio telescopes spread across the United States, with baselines ranging from approximately 200 km to 8,611 km, spanning from Mauna Kea, Hawaii, to St. Croix in the U.S. Virgin Islands. Each station is equipped with a

25-meter radio antenna and facilities for recording and processing data. The configuration of the VLBA is shown in Figure 2.1. The VLBA is sensitive to emission from sources with very high brightness temperatures ($T_B > 10^6$ K) and is therefore ideal for detecting objects undergoing non-thermal processes, such as the magnetically active YSOs discussed in Section §1.3.1. The VLBA achieves angular resolutions of approximately 1 milli arcsecond and astrometric precisions on the order of 100 micro arcseconds, making it an invaluable tool for studying binary systems in star-forming regions (Reid & Honma, 2014). In these regions, the VLBA has been employed to measure proper motions and trigonometric parallaxes of magnetically active young stars through multi-epoch observations (Loinard et al., 2005; Menten et al., 2007; Dzib et al., 2010, 2011, 2016, 2018). These measurements have enabled detailed mapping of the three-dimensional structure and kinematics of molecular clouds. A notable project in this context is the *Gould's Belt Distances Survey* (GOBELINS), which aimed to determine the distances to several dozen young stars in star-forming regions. Thanks to studies conducted with the VLBA, the distances to the nearest and most prominent star-forming regions are now known with better than 5% accuracy (Ortiz-León et al., 2017b,a, 2018a; Kounkel et al., 2017; Galli et al., 2018).

2.2 Observational Data

The data used for the development of this thesis are part of the *Dynamical Masses of Young Stellar Multiple Systems with the VLBA* (DYNAMO-VLBA[1], P.I.: S. Dzib, project code: BD215). This project aimed to monitor 20 known close binary systems and one triple system, distributed across prominent nearby star-forming regions, including Ophiuchus, Serpens, Taurus, and Orion. The primary objective was to refine their orbital parameters and measure the dynamical masses of their components, enabling direct comparisons with theoretical models of early stellar evolution. The observations were conducted at a central frequency of 5.0 GHz (C-band, λ = 6.0 cm) between February 2018 and January 2021.

Further, the DYNAMO-VLBA data were complemented by archival observations from the GOBELINS project (Loinard et al., 2008; Ortiz-León et al., 2017b,a, 2018b), which provided

[1] https://www3.mpifr-bonn.mpg.de/div/radiobinaries/intro.php

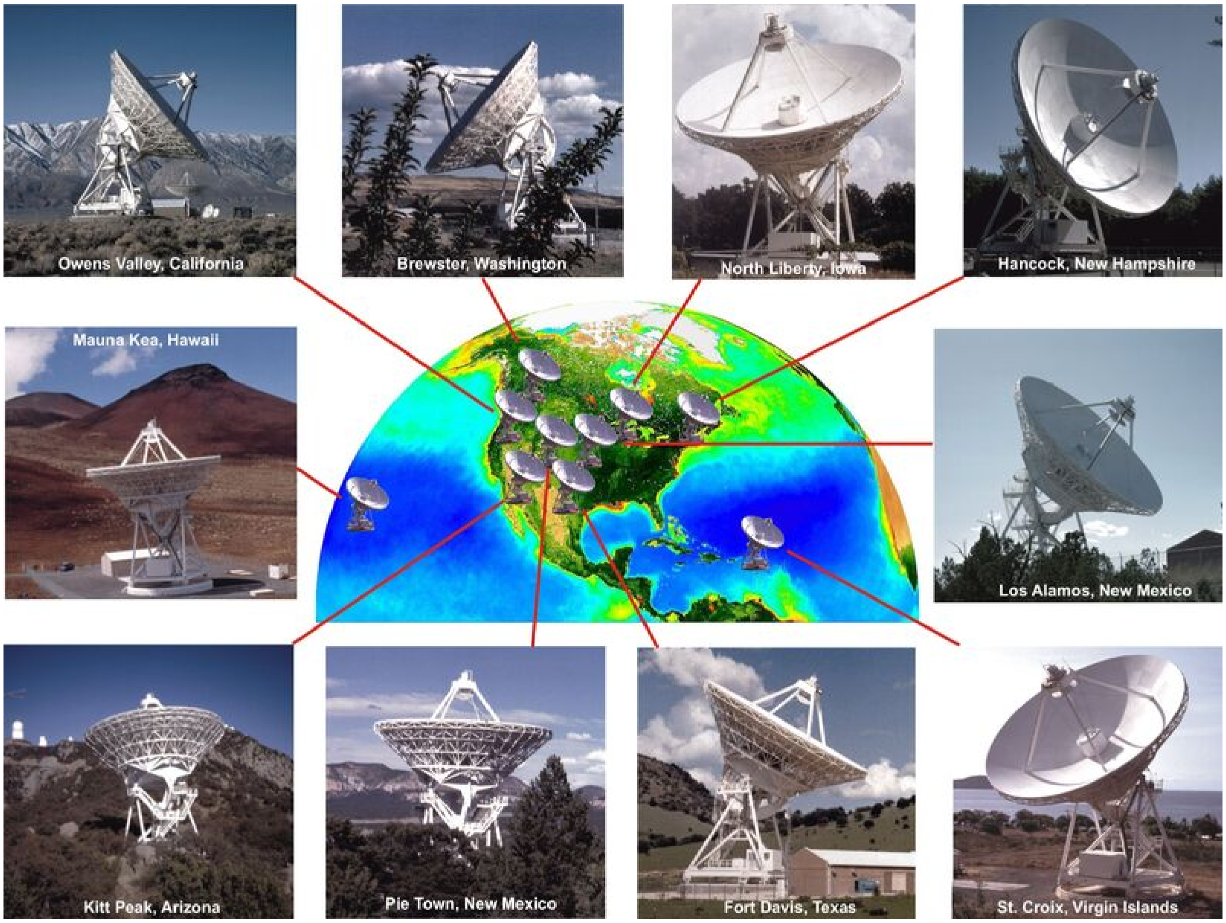

Figure 2.1: Configuration of the Very Long Baseline Array (VLBA). Credits: NRAO/AUI, Earth image courtesy of the SeaWiFS Project NASA/GSFC and ORBIMAGE.

precise distances to several YSOs in these regions. Additionally, new VLBA observations were conducted under the project code BO072 (P.I.: J. Ordoñez-Toro), carried out between September 2023 and July 2024, as detailed in Chapter 4.

This thesis focuses on binary systems composed of intermediate-mass stars located in the nearby star-forming regions of Ophiuchus and Serpens described in Section §1.2. Specifically, the systems S1 in Ophiuchus and EC 95 in Serpens were selected for detailed analysis due to their accessibility for high-precision astrometric monitoring. As discussed in Chapters 3, 4, and 5, these systems provide valuable insights into the orbital dynamics and masses of young low- and intermediate-mass stars.

2.3 Data Calibration

The calibration of the data is performed using the Astronomical Image Processing System (AIPS) software package (Greisen, 2003), following standard procedures for phase-referenced VLBI observations as described in Loinard et al. (2007), Dzib et al. (2010), and Ortiz-León et al. (2017b). The calibration process involves applying a series of corrections to the amplitude and phase of the interferometric visibilities, accounting for atmospheric, ionospheric, and instrumental effects that can affect the quality and accuracy of the measurements.

The first step is to apply ionospheric corrections to account for delays caused by the Earth ionosphere, which contains free electrons that introduce frequency-dependent phase errors and distort the observed signals. To correct for these ionospheric delays, models based on Global Positioning System (GPS) measurements are used to estimate the total electron content along the line of sight. Subsequently, corrections are made for instrumental effects and inaccuracies in the Earth orientation parameters. Errors in the initial atmospheric models used by the VLBA correlator and clock inaccuracies at each antenna (Reid & Brunthaler, 2004) are addressed by updating the EOPs—refining the predicted values originally used by the correlator with more accurate measurements to better account for the rotation and orientation of the Earth.

Instrumental delays and phase offsets between different antennas are corrected using calibration data from known strong sources. This involves observing a nearby phase calibrator source with a well-known position at regular intervals during the observation of the target source. Since the calibrator is assumed to be a point source with stable flux and position, it serves as a reference to correct for time-varying phase errors due to atmospheric fluctuations and instrumental instabilities. Residual delay errors are refined using the DELZN task, which corrects for any remaining timing discrepancies, while the ATMCA task is applied to mitigate phase variations caused by atmospheric effects. The derived delay and phase corrections are then interpolated to the target sources. Amplitude calibration is performed using measurements of the system temperature and standard gain curves provided by each antenna, ensuring that the flux densities of the sources are accurately determined for meaningful comparisons across observations.

Once calibration is complete, the data are transformed into images using Fourier inversion and deconvolution techniques. This imaging process converts the calibrated visibility data into sky maps that reveal the brightness distribution of the sources. Flux densities and positions of the detected sources are determined by fitting two-dimensional Gaussian models to the images using the AIPS task `JMFIT`. This process provides precise estimates of the source parameters, including peak flux density, integrated flux, position, and deconvolved source size.

An additional step that can be performed when a source exhibits a stable and sufficiently bright brightness distribution is self-calibration. This technique improves the final image quality by iteratively correcting residual phase and amplitude errors that remain after the initial calibration. The process begins with the generation of an initial image and model from the calibrated data, followed by successive refinements based on comparisons between the observations and the model. This iterative process increases signal coherence, reduces noise, and enhances both the image fidelity and dynamic range, thereby enabling the detection of weak sources that might not be apparent after the initial calibration.

The detailed calibration and data reduction processes for each system are described in the *Observations and Data Reduction* sections in the following chapters, corresponding to each of the papers included in this thesis.

2.4 Orbital Dynamics and Data Fitting

To study the dynamics of orbital motion in a binary system, it is necessary to consider the orbital elements that describe its geometry and orientation. These parameters are directly related to the equations of motion that govern the observed positions of the stars. In a binary system, each component follows an elliptical orbit, with the center of mass located at one focus of the ellipse, as illustrated in Figure 2.2. The following outline provides a brief overview of the analysis of binary systems, following the methodologies described by Carroll & Ostlie (1996); Karttunen et al. (2017); Perryman (2018).

In general, to describe the trajectory of one of the stars in an elliptical orbit, the following

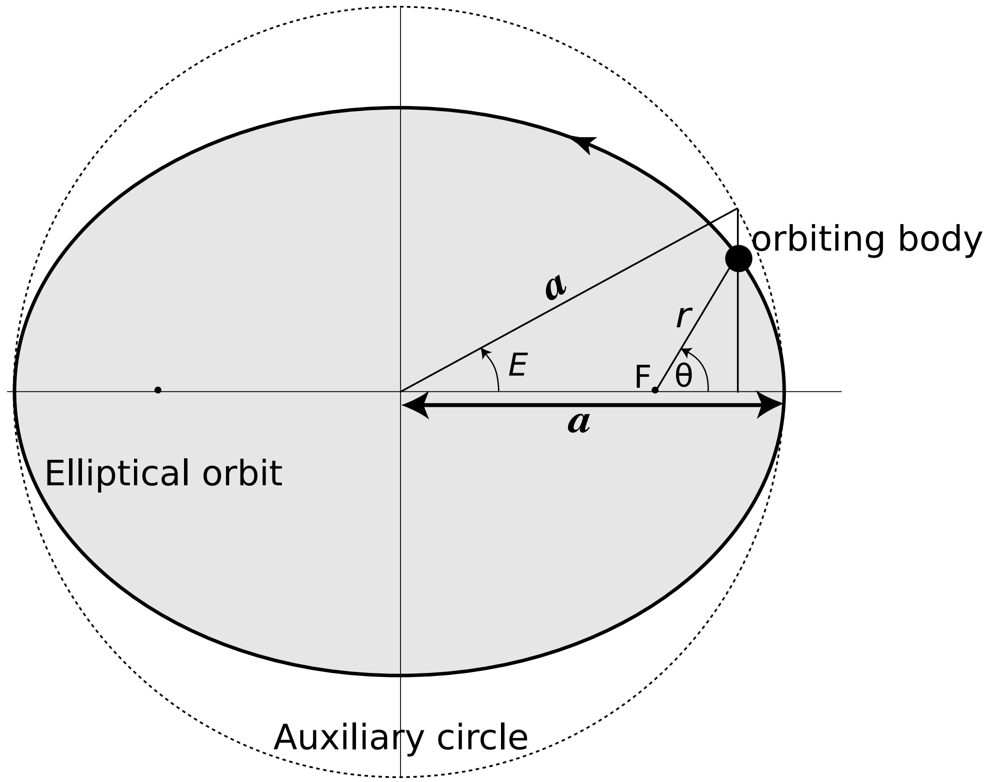

Figure 2.2: Geometry of an elliptical orbit, where the position along the orbit is characterized either by the true anomaly θ (measured with respect to the ellipse) or by the eccentric anomaly E (defined on an auxiliary circle with a radius equal to the semi-major axis a). The focus F represents the center of mass of the system. This figure is adapted from Figure 2.1 in Perryman (2018).

parameters are defined, which are illustrated in Figure 2.2:

- **Semi-major Axis (a):** Half the length of the major axis of the ellipse, which sets the scale of the orbit.

- **Orbital Period (P):** Specifies the time required for the star to complete one full orbit.

- **Eccentricity (e):** Quantifies the shape of the orbit; $e = 0$ corresponds to a circular orbit, while $0 < e < 1$ corresponds to an ellipse.

- **True Anomaly (θ):** The angle between the direction of periastron and the instantaneous position of the star along its orbit, measured from the center of mass. This parameter varies with time and indicates the current location of the star along its elliptical path.

- **Eccentric Anomaly (E):** An auxiliary angle defined on the circle with radius a that facilitates the link between position and time.

Finally, to complete the description of the dynamics of the orbit, the three-dimensional orientation is specified by the following angular parameters, as illustrated in Figure 2.3:

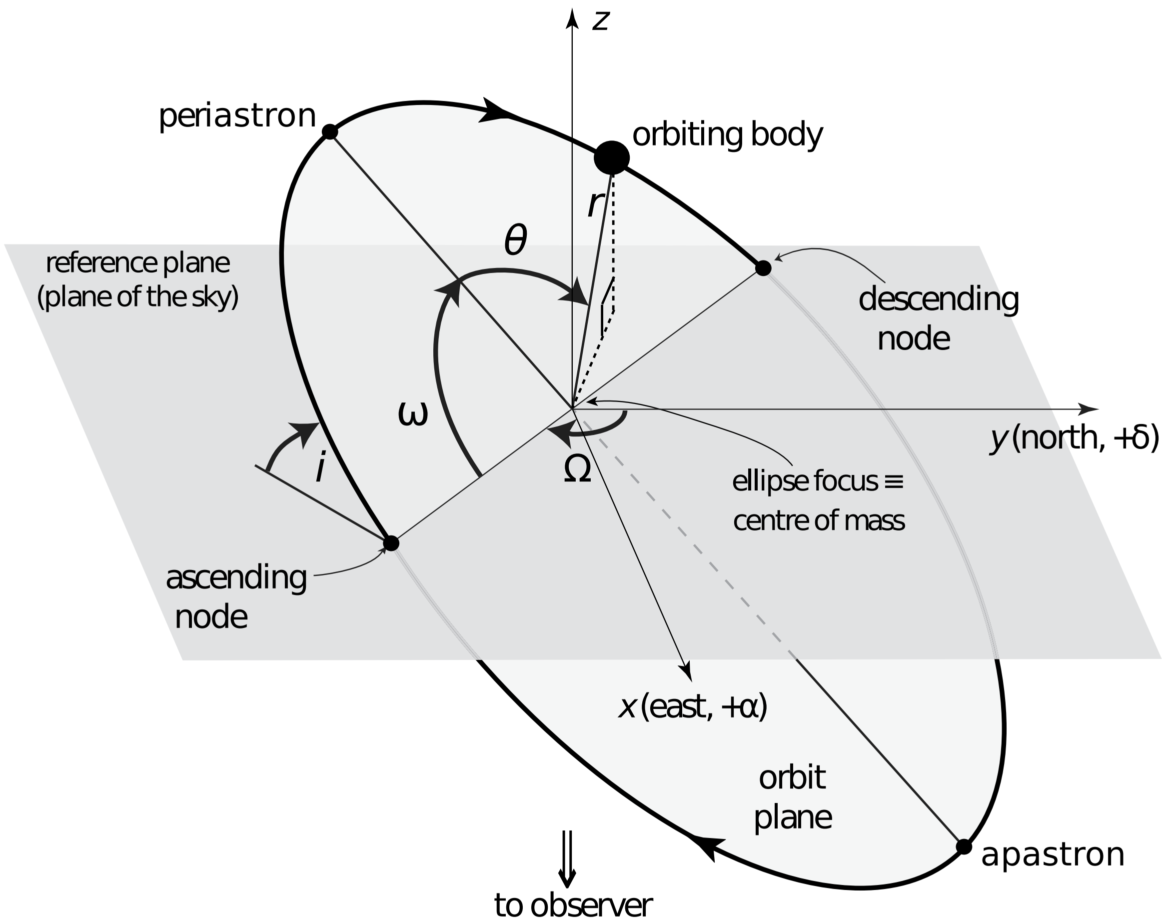

Figure 2.3: Diagram of an elliptical orbit with its main orbital elements. This diagram, adapted from Figure 2.2 in Perryman (2018), employs a right-handed coordinate system in which the x-axis is directed eastward (with increasing α), the y-axis northward (with increasing δ), and the z-axis extends away from the observer. In this representation, the y-axis serves as the reference axis, which contrasts with the solar system convention that uses the x-axis aligned with the vernal equinox, as the reference.

- **Inclination (i):** This angle describes the tilt of the orbital plane relative to a fixed reference plane. An inclination of $i = 0°$ indicates a face-on orbit, while $i = 90°$ indicates an edge-on orbit. For objects moving in a counterclockwise direction, i ranges from 0° to 90°; for retrograde (clockwise) orbits, i lies between 90° and 180°.

- **Longitude of the Ascending Node (Ω):** The angle measured in the reference plane (typically relative to north) from a fixed direction to the ascending node, where the star crosses the reference plane from below to above.

- **Argument of Periastron (ω):** The angle in the orbital plane measured from the ascending node to periastron (the point of closest approach to the center of mass). In the case of the secondary component, ω differs by 180° with respect to the primary, reflecting the symmetry of the motion about the center of mass.

2.4.1 Dynamical Mass Estimation in Binary Systems

To study the detailed orbital dynamics of binary systems, Kepler's laws are employed to describe the motion of both stars. In the previous section, a brief description was given of the orbital elements that characterize this motion and how their positions are determined. In particular, if the absolute size of the orbit and the distance to the system are known, Kepler's third law allows for the calculation of the total mass of the system:

$$M = M_1 + M_2 = k\,\frac{(a_1 + a_2)^3}{P^2}\,, \tag{2.1}$$

where a denotes the semi-major axis of the relative orbit (with $a = a_1 + a_2$), M is the total mass of the system, $k = \dfrac{4\pi^2}{G}$ (with G being the gravitational constant), and P is the orbital period.

Determining the individual stellar masses in a binary system depends on precise measurements of the orbital parameters. By observing the motion of both stars relative to the center of mass, high-precision astrometric data yield the semi-major axes of their orbits. Consider a binary system with masses M_1 and M_2, where the stars orbit their common center of mass in elliptical orbits, as shown in Figure 2.4. Assuming that the orbital plane is perpendicular to the line of sight, the angles subtended by the semi-major axes are α_1 and α_2. If the distance from the observer to the system is d, then the semi-major axes are determined by $a_1 = \alpha_1\, d$ and $a_2 = \alpha_2\, d$.

The mass ratio can be determined with respect to the semi-major axes as follows:

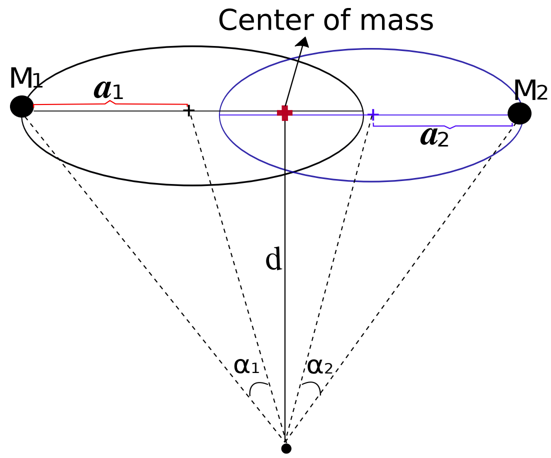

Figure 2.4: Orbital motion of the components of a binary system around their common center of mass. This figure is adapted from the Binary Stars and Stellar Masses section by Karttunen et al. (2017).

$$M_1\, a_1 = M_2\, a_2 \quad \Longrightarrow \quad \frac{M_1}{M_2} = \frac{a_2}{a_1} = \frac{\alpha_2}{\alpha_1}\,. \tag{2.2}$$

Finally, combining this relation with Equation 2.1, and expressing it in terms of the observables, the individual masses of each component are calculated as:

$$M_1 = k\, \frac{(\alpha_1 + \alpha_2)^2\, \alpha_2\, d^3}{P^2}, \quad M_2 = k\, \frac{(\alpha_1 + \alpha_2)^2\, \alpha_1\, d^3}{P^2}\,. \tag{2.3}$$

2.4.2 Astrometric and Orbital Fitting

The movement of stars in binary systems is fundamentally described by their displacements on the celestial sphere over time. These displacements result from a combination of their common trigonometric parallax π, the uniform proper motion of their center of mass in right ascension and declination, μ_α and μ_δ, and their orbital motion. To better understand this, it is necessary to analyze both the astrometric and orbital parameters that define and govern these motions, as described below.

The observed position of each star in a binary system as a function of time can be expressed in terms of astrometric and orbital parameters:

$$\alpha(t) = \alpha_0 + (\mu_\alpha \cos\delta)t + \pi f_\alpha(t) + Q_\alpha(t), \tag{2.4}$$

$$\delta(t) = \delta_0 + \mu_\delta t + \pi f_\delta(t) + Q_\delta(t), \tag{2.5}$$

where α_0 and δ_0 are the coordinates of the center of mass of the system at the chosen reference epoch, f_α and f_δ are the projections of the parallactic ellipse (Seidelmann, 1992). $Q_\alpha(t)$ and $Q_\delta(t)$ represent the projections of the orbital motions and are functions of the orbital elements:

$$Q_\alpha(t) = r\left[\cos(\theta+\omega)\sin\Omega - \sin(\theta+\omega)\cos\Omega\cos i\right]/\cos\delta, \tag{2.6}$$

$$Q_\delta(t) = r\left[\sin(\theta+\omega)\sin\Omega\cos i + \cos(\theta+\omega)\cos\Omega\right], \tag{2.7}$$

where the true anomaly θ and the orbital elements (i, Ω, and ω) have been previously defined. The distance r of the primary component from the center of mass, which in polar coordinates is defined as:

$$r = \frac{a_1(1-e^2)}{1+e\cos\theta}\,. \tag{2.8}$$

The geometric relation between the true anomaly θ and the eccentric anomaly E is expressed as:

$$\theta = 2\tan^{-1}\left(\sqrt{\frac{1+e}{1-e}}\,\tan\frac{E}{2}\right). \tag{2.9}$$

The contribution of the orbital motion to the displacement of each component at a given epoch t is determined using the orbital parameters, the epoch of periastron passage T_0, and the mean anomaly $\mathcal{M}$, defined as:

$$\mathcal{M} = \frac{2\pi}{P}(t-T_0)\,, \tag{2.10}$$

The relation between the mean anomaly and the eccentric anomaly is given by Kepler's equation:

$$\mathcal{M} = E - e\sin E\,. \tag{2.11}$$

Once E is determined, the true anomaly θ and the distance r can be calculated using Equations 2.9 and 2.8.

For the secondary component, the semi-major axis a_2 replaces a_1 in equation (2.8), which is scaled from a_1 by the mass ratio, and the true anomaly θ is rotated 180° in equations (2.6) and (2.7) (e.g., Kounkel et al. 2017). This adjustment reflects that the two stars occupy opposite positions relative to the center of mass. This set of equations provides a detailed way to model the orbital and astrometric motion in binary systems.

To solve these equations and derive the orbital and astrometric parameters, two different methods were employed. These were selected to address the characteristics of the available data and to compare the results obtained through distinct approaches. The methods used in the analysis of this thesis are described below:

* **Full stellar motion using MPFIT**

To implement this framework and solve the equations (2.8)–(2.7), we employed a Python implementation of the MPFIT algorithm by Kounkel et al. (2017)[2]. MPFIT is a robust non-linear least-squares fitting routine based on the *Levenberg-Marquardt method*, originally developed as part of the MINPACK-1 package (Markwardt, 2009). This algorithm minimizes the chi-squared statistic, defined as:

$$\chi^2 = \sum_i \frac{(y_i - f(x_i, \mathbf{p}))^2}{\sigma_i^2},$$

where y_i are the observed data points, $f(x_i, \mathbf{p})$ is the model function with parameters $\mathbf{p}$, and σ_i represents the uncertainties of the measurements.

This routine iteratively minimizes the residuals between observed and modeled data, ensuring an optimal fit to the complex equations describing the motion of binary systems. This routine simultaneously fits equations (2.4) and (2.5) to the data, incorporating both absolute positions of both stars from VLBA astrometry and relative positions derived from optical or near-infrared imaging, when available. By combining these data sets, the routine allows for comprehensive modeling of proper motion, parallactic motion, and orbital motion.

The free orbital parameters in this model include the period P, the semi-major axis of the orbit of the primary star a_1, the eccentricity e, the inclination i, the position angle of the

[2] The full routine is available at https://github.com/mkounkel/astrometric_binaries/blob/master/astrometry_binary_python3.ipynb

ascending node Ω, the argument of periastron ω, the time of periastron passage T, and the mass ratio M_2/M_1. The total mass of the system is derived using the third law of Kepler, combined with the distance obtained from the trigonometric parallax included in the same fit.

The Levenberg-Marquardt algorithm combines the stability of gradient descent when far from the solution with the efficiency of the Gauss-Newton method when near convergence. It dynamically adjusts its damping factor to balance these two techniques, ensuring robust performance even for non-linear models like those used in orbital fitting. However, this routine is sensitive to the initial guesses of certain non-linear parameters, particularly P, e, ω, and Ω. Poor initial guesses may lead the fitter to converge to a local minimum instead of the global minimum. To address this, the fitting process is repeated 1000 times with different initial guesses for these parameters, thoroughly exploring the parameter space. The algorithm iterates over these guesses, achieving optimal convergence in many of the iterations.

The best solutions are identified based on their goodness of fit, measured by the reduced chi-squared (χ^2) statistic. Iterations with $\chi^2 < 1.1\chi^2_{\text{best}}$ (where χ^2_{best} is the minimum chi-squared value across all iterations) are selected for further analysis. Parameter uncertainties are evaluated in two ways: examining the intrinsic scatter among all valid solutions, and calculating a weighted average of the errors returned by MPFIT, weighted by their respective (χ^2) values. Both methods yield consistent results, ensuring robust estimates of parameter uncertainties. This procedure enables the precise determination of key orbital parameters, dynamical masses, and trigonometric parallaxes. The ability to simultaneously fit absolute and relative astrometric data makes this approach highly effective for modeling binary systems.

$*$ **Orbital Fitting Using `Orbitize!`**

As a complementary step to confirm and refine the orbital parameters obtained with MPFIT, we used the `Orbitize!`[3] package, an open-source, object-oriented Python tool specifically designed for fitting orbits in binary and exoplanetary systems (Blunt et al., 2017, 2020). `Orbitize!` integrates two advanced statistical methodologies: *Orbits for the Impatient* (OFTI) and *Markov*

[3] `https://orbitize.info/en/latest/`

Chain Monte Carlo (MCMC), which allow for efficient exploration of the multidimensional orbital parameter space within a Bayesian framework.
The orbital dynamics in `Orbitize!` are modeled using the classic two-body problem, where the relative positions of the secondary with respect to the primary in the plane of the sky are calculated by solving Kepler equation 2.11. To solve this equation, `Orbitize!` employs two numerical methods depending on the value of e:

- **Newton Method:** Used for eccentricities $e < 0.95$, this iterative approach is computationally efficient for low to moderate eccentricities.

- **Mikkola Method:** Designed to handle eccentricities close to 1, this algorithm combines an initial cubic approximation with a precise correction, ensuring stability and efficiency for extreme cases (Mikkola, 1987).

After solving Kepler equation to calculate θ, `Orbitize!` directly fits the resulting relative positions of the secondary using a Bayesian orbital fitting process. This process incorporates two complementary approaches designed to accommodate different types of observational data:

- **OFTI (Orbits for the Impatient):** OFTI is a rejection-sampling algorithm that generates and evaluates a large number of orbits quickly and efficiently. It starts with reasonable prior distributions for the orbital parameters, and each generated orbit is scaled and rotated to align with the most restrictive observations. The quality of each orbit is evaluated using a likelihood metric, such as χ^2, retaining only those orbits with acceptable probabilities. This method is particularly effective when observations cover a small fraction of the orbital period, allowing for rapid exploration of the parameter space without requiring precise initial guesses (Blunt et al., 2017).

- **MCMC (Markov Chain Monte Carlo):** To refine the posterior distributions, `Orbitize!` implements two MCMC variants: the *Affine-invariant* sampler from `emcee` (Foreman-Mackey et al., 2013) and the *Parallel-tempered* sampler from `ptemcee` (Vousden et al., 2016). The latter is optimized for handling multimodal distributions and complex correlations. During this stage, a large ensemble of walkers iteratively explores the parameter space after a burn-in phase to ensure convergence of the chains. Additionally, well-determined values, such as the parallax derived from MPFIT, are fixed to improve the stability and precision of the posterior distributions.

Unlike the MPFIT-based method, which fits absolute positions and allows for the derivation of individual masses, `Orbitize!` uses relative positions from observations where both components were simultaneously detected. This means that parameters like parallax must be fixed externally (in this case, using the value obtained with MPFIT), and the method only returns the total mass of the system, without resolving individual masses. On the other hand, `Orbitize!` handles errors more rigorously, making it particularly suitable for analyzing precise observations such as those from VLBA. The final results showed excellent agreement with those obtained using MPFIT, validating the robustness and consistency of both methods.

2.5 Spectral Energy Distribution Analysis

The SED is a fundamental tool for deriving the physical properties of YSOs, including effective temperature, luminosity, and stellar radius. As mentioned in Section §1.3, YSOs are often embedded in dense molecular clouds, where interstellar dust causes reddening and attenuation of their emission. This effect depends on wavelength and can alter the shape of the observed SED. To correct for the effects of dust, extinction models are used, which account for the interaction of light with dust along the line of sight and help recover the intrinsic emission of these systems.

One of the simplest methods for fitting the observed SED of a star is by using a reddened blackbody spectrum. This model combines a blackbody emission curve, representing the stellar photosphere, with an extinction correction curve that describes wavelength-dependent attenuation caused by dust. Commonly used extinction models include the laws of Fitzpatrick (1999) and Fitzpatrick et al. (2019), which are ideal for correcting extinction in the optical and near-infrared regimes of the Milky Way. For the near- to mid-infrared, it is common to employ the Rieke et al. (1989) extinction law, which captures the properties of dust in regions with significant infrared emission, such as those surrounding YSOs. These models incorporate parameters related to extinction, such as reddening $E(B-V)$, the total-to-selective extinction ratio in the optical $R_V \equiv A_V/E(B-V)$, and the total extinction in the V band, with $R_V = 3.1$

being the typical value for the Milky Way.

The main motivation for performing these SED adjustments is to determine the effective temperature, luminosity, and stellar radius. These parameters make it possible to locate stars in the Hertzsprung-Russell diagram and, therefore, determine the masses predicted by pre-main sequence stellar evolution models, as described in Section §1.5. This analysis is crucial for assessing the consistency between dynamical masses measured and theoretical model predictions. For this reason, we include the SED analysis for the sources studied in this thesis, S1 and EC 95, as detailed in Sections §3 and §5, respectively. In general terms, for this analysis, we used the Python package `dust_extinction`, which provides models of interstellar dust extinction curves[4]. This package includes the aforementioned models and allows for their application. The SED fitting process begins with the compilation of photometric observations available from the VizieR astronomical catalog service. These data are modeled using a reddened blackbody function combined with appropriate extinction laws. The fitting process is designed according to the characteristics of each source, meaning that the strategy is adapted based on the available constraints. Specifically, well-constrained parameters are fixed while optimizing the remaining ones. For instance, in the case of the EC 95 system, the effective temperature (T_{eff}) is derived from high-resolution spectroscopy and is kept fixed, allowing the stellar radius (R) and extinction (A_V) to be treated as free parameters. Similarly, for the S1 system, both the effective temperature and stellar radius are fixed within a range determined by spectral type calibrations from Pecaut & Mamajek (2013), leaving A_V as the only free parameter in the fit.

The script developed for this analysis explores a range of possible values for the free parameters and calculates theoretical fluxes by combining the blackbody model with extinction laws. It then computes the squared residuals between the observed and theoretical fluxes across the wavelength range. Finally, the total residuals are minimized to determine the best-fitting parameters, ensuring the most accurate reconstruction of the SED.

[4] `https://dust-extinction.readthedocs.io/en/stable/index.html` for more details

Chapter 3

Dynamical Mass of the Oph-S1 Binary System

This chapter includes the first paper of this thesis, titled ***Dynamical Mass of the Ophiuchus Intermediate-Mass Stellar System S1 with DYNAMO-VLBA*** (Ordóñez-Toro et al., 2024). It presents a comprehensive analysis of the dynamical masses of the individual stars in the nearby young binary system S1. As previously discussed in Section §1.2, this system is the most massive and luminous member of the Ophiuchus star-forming region and is located in the dense core of the molecular cloud Lynds 1688 (L1688). Observations from infrared lunar occultation (Richichi et al., 1994) and VLBA radio data (Ortiz-León et al., 2017b) have confirmed that S1 is a binary system, with components separated by an angular distance of approximately 20 to 30 milliarcseconds. Both stars, designated as S1A (the primary) and S1B (the secondary), are non-thermal radio emitters. Since S1 is the most massive stellar member of Ophiuchus, it represents a key object for studying the early evolution of intermediate-mass stars in nearby binary systems. Previous studies have classified S1 as a B3–B5 spectral type star (e.g., Lada & Wilking, 1984; Wilking et al., 2005), with an estimated mass of approximately 5–6 $M_{\odot}$. Additionally, Ortiz-León et al. (2017b) obtained preliminary dynamical masses of 5.78 ± 0.15 $M_{\odot}$ for S1A and 1.18 ± 0.10 $M_{\odot}$ for S1B.

In this study, I analyzed 35 VLBA observations spanning 2005 to 2019, including 28 archival data sets from the GOBELINS project (Ortiz-León et al., 2017b) and seven recent observations from the DYNAMO-VLBA project. The primary goal was to precisely determine the astrometric and orbital parameters of the S1 system, enabling accurate dynamical mass measurements of its components. Data calibration, described in detail in Section §2.3, was carried out using the AIPS software. Additionally, self-calibration was applied for each epoch by performing phase and amplitude corrections using the source as a model. This process significantly improved the detection of S1B, allowing it to be identified in more epochs than previously reported. Furthermore, we verified that an earlier reported detection of S1B on June 3, 2006 (Ortiz-León et al., 2017b) was actually a prominent sidelobe rather than a true detection of the secondary component. S1A was consistently detected in all 35 epochs, including those reported in earlier studies (Loinard et al., 2008; Ortiz-León et al., 2017a, 2018b), while S1B was detected in a total of 14 epochs. The astrometric fitting was performed using specialized routines, including MPFIT, implemented in Python by Kounkel et al. (2017), which enabled precise determination of the orbital parameters and individual masses of both stars (see Section §2.4.2). To further evaluate the robustness of the orbital parameters obtained from the least-squares fit, we employed the *Orbitize!* package (Blunt et al., 2017). This software uses a *Markov Chain Monte Carlo* (MCMC) algorithm to explore the parameter space comprehensively, compute posterior distributions for the orbital parameters, and validate the results of the initial fitting, as discussed in Section §2.4.2.

The results show that the primary component, S1A, has a mass of $4.112 \pm 0.099\, M_{\odot}$, which is significantly lower than the previously suggested value of approximately $6\, M_{\odot}$, based on its spectral type (Andre et al., 1988; Wilking et al., 2005). In contrast, the secondary component, S1B, has a mass of $0.831 \pm 0.014\, M_{\odot}$, consistent with a low-mass young star. This discrepancy with the values reported by Ortiz-León et al. (2017b) can be attributed to the larger number of S1B detections in our study. While Ortiz-León et al. (2017b) reported only four detections of S1B, our analysis includes a total of 14 detections, leading to improved orbital constraints and more precise dynamical mass estimates.

To compare the predicted masses from pre-main sequence stellar evolution models with the dynamical measurements obtained in this study, we analyzed the SED of S1A to reevaluate its effective temperature and luminosity. Using photometric data from the VizieR database, the SED was fitted with a reddened blackbody model, employing extinction curves from Fitzpatrick (1999) and Rieke et al. (1989), this process was described in Section §2.5. For this case, the effective temperature $T_{\rm eff}$ and stellar radius R were fixed based on the previously reported B3–B5 spectral type (Lada & Wilking, 1984). The corresponding $T_{\rm eff}$ and R values for B3, B4, and B5 were adopted from the spectral type calibrations by Pecaut & Mamajek (2013). The best-fit model indicated that S1A can be characterized as a reddened blackbody with an $T_{\rm eff}$ between $14,000$ and $17,000$ K, consistent with a B3-B5 spectral type. Based on these results, we evaluated several pre-main sequence stellar evolution models, including the PISA model (Tognelli et al., 2011), which suggests that the luminosity and effective temperature derived from the SED of S1A correspond to a mass between 5 and 6 $M_{\odot}$, significantly higher than the dynamical mass of 4.1 $M_{\odot}$. For completeness, additional models, such as the Y^2 (Yonsei-Yale) models (Yi et al., 2001), Palla-Stahler models (Palla & Stahler, 1999), PARSEC models (Nguyen et al., 2022), and YaPSI (YALE-POTSDAM) models (Spada et al., 2017), were tested. Each of these models is described in detail in Section §1.5, and all of them consistently produced conclusions similar to those of the PISA model. Consequently, we conclude that pre-main sequence evolutionary models overestimate the mass of the intermediate-mass star S1A by 20 to 50%.

According to the pre-main sequence evolutionary models, the location of S1A in the HR diagram—above and to the right of the main sequence—indicates that the star has not yet reached that phase. Since intermediate-mass stars have a very short pre-main sequence lifetime, this imposes strict constraints on the age of the S1 system. For example, according to the evolutionary models of Tognelli et al. (2011), a 5 M$\odot$ star reaches the main sequence in approximately 1 Myr. The possible location of S1A along the track of a 5 M$\odot$ star suggests an age of 0.7 Myr, as indicated by these models. However, as noted earlier, the models do not reproduce the location of S1A in the HR diagram given its dynamically measured mass; therefore, caution must be exercised when deriving age estimates from them. Consequently, we conclude that the age of S1A is probably between 0.5 and 1 Myr.

We also analyzed the flux density variations of S1A and S1B as a function of their orbital phase and identified a significant correlation for S1B, with radio flux increasing near apastron. Specifically, S1B was detected in 64% of the observations taken between orbital phases 0.4 and 0.6, i.e., near apastron, but only in 24% of observations outside this phase range. In contrast, the flux density of S1A remained stable throughout the orbit. This observation led us to explore several hypotheses, including the possibility of an optically thick region around S1A that could absorb the emission from S1B when the stars are within 20 mas of each other. However, this would require a specific morphology, such as a toroid with an inner gap, to avoid affecting the emission from S1A. We conclude that the origin of this behavior is unclear.

Finally, a comparison between VLBA radio astrometry and Gaia DR3 data reveals that while the Gaia position is close to, it does not coincide with the position of S1A as measured by the VLBA. This offset is expected, as Gaia observes the motion of the photocenter of the system, likely dominated by the primary star, S1A. Since Gaia cannot resolve the system or account for its orbital motion, its parallax measurement is significantly less accurate and only marginally consistent with the VLBA result. These findings underline the unique capabilities of the VLBA for resolving this type of system with high precision, making it a valuable complement to Gaia.

- **keywords:** Binary stars, astrometry, dynamical masses, VLBA, star:formation, intermediate-mass stars.

- **Article Reference:** The complete article, detailing the methods and results of this study, can be accessed at the following link: DOI:10.3847/1538-3881/ad1bd3.

Chapter 4

Confirmation of Oph-S1 Orbital elements and Mass

This chapter includes the second paper of this thesis, titled *VLBA Detections in the Oph-S1 Binary System near Periastron: Confirmation of its Orbital Elements and Mass* (submitted to the *MNRAS* journal). Building on the study of the Ophiuchus S1 binary system presented in Chapter 3, this work addresses the challenges in detecting the secondary component, S1B, near periastron. The variability in the radio flux of S1B reported in the first paper motivated a new series of observations designed to enhance detection capabilities during this critical orbital phase. Using the orbital model established in Ordóñez-Toro et al. (2024), which accurately predicted the timing of the next periastron passage, we proposed and conducted targeted VLBA observations to improve sensitivity and phase coverage.

The new observations were carried out under VLBA project code BO072 (P.I.: J. Ordoñez-Toro) between September 2023 and June 2024. This campaign adopted the successful strategies developed in the GOBELINS (P.I.: L. Loinard) and DYNAMO-VLBA (P.I.: S. Dzib) projects but included modifications to increase the likelihood of detecting S1B. Specifically, the integration time was extended to 120 minutes per epoch (on-source), and monthly observing intervals were implemented to provide detailed coverage of the orbital phase from $\phi = 0.8$ to $\phi = 0.2$, passing through periastron at $\phi = 0.0$. This approach yielded nine epochs, totaling 36 hours of observation time.

Data calibration and self-calibration were performed using the AIPS software, as described in earlier sections. These new observations, combined with archival data from the GOBELINS and DYNAMO-VLBA projects, expanded the dataset to 44 epochs spanning 19 years. This extensive dataset enabled a comprehensive orbital analysis, including precise astrometric and orbital fitting using MPFIT (Kounkel et al., 2017). The updated results confirmed the masses of S1A at 4.115 ± 0.039 $M_\odot$ and S1B at 0.814 ± 0.006 $M_\odot$, with significantly improved precision compared to previous measurements.

The new observations allowed detections of S1B at phases as close to periastron as $\phi \simeq 0.002$, ruling out the hypothesis that an optically thick region around S1A absorbs the emission of S1B at that phase. A total of 44 observations were recorded, from which 19 detections were obtained, corresponding to an overall detection rate of approximately 43.2%. However, a phase-segmented analysis reveals notable differences in the detectability of S1B. In the apastron range ($0.4 \leq \phi \leq 0.6$), the detection rate remains similar to that reported in (Ordóñez-Toro et al., 2024), reaching around 60.0% ± 12.6% (9 detections out of 15 observations), as new observations were primarily focused on periastron to improve coverage. The uncertainty corresponds to the standard error of a proportion, calculated as $\mathrm{SE}(p) = \sqrt{p(1-p)/n}$.
In the periastron range ($\phi \leq 0.2$ or $\phi \geq 0.8$), the detection rate is 33.3% ± 16.5% (5 detections in 15 observations), as shown in the top panel of Figure 4.1. If the detectability of S1B is modeled with a binomial distribution, a global probability of $p \approx 0.432$ is obtained (see Section 4.2 of (Ordóñez-Toro et al., 2024)). According to this model, the probability of obtaining 9 detections in 15 observations at apastron is 9%, while at periastron, the probability of obtaining 5 detections in 15 observations is 16%. These values suggest that, if detectability were independent of phase, the observed distribution of detections would still be unlikely to occur purely due to random fluctuations.

It is important to note that, although the new observations applied higher sensitivity at periastron through monthly monitoring to compensate for the shorter transit time in that phase, the number of available observations remains limited. As a result, the detection rate at periastron remains lower than at apastron, as shown in the bottom panel of Figure 4.1. This supports the idea that S1B is intrinsically more detectable at apastron.

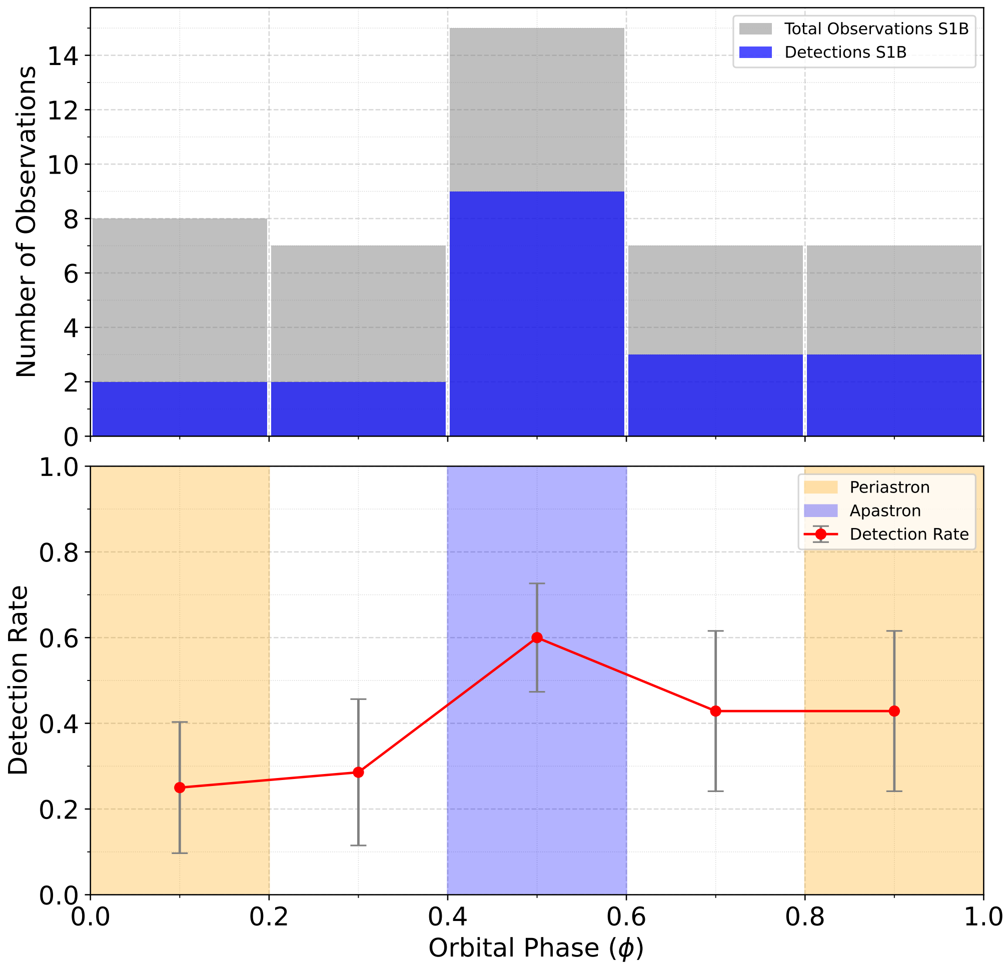

Figure 4.1: Histogram of the total number of observations and detections of S1B as a function of orbital phase (top) and detection rate as a function of orbital phase (bottom), both in bins of 0.2.

Regarding the results of the astrometric and orbital parameters, we find that they have been refined in this work, leading to a more precise characterization of the system. Additionally, the mass estimates have been improved, further consolidating S1A as an intermediate-mass young star with a mass 25% lower than earlier photometric estimates and confirming S1B as a low-mass T Tauri star. These findings provide valuable insights into binary star dynamics near periastron and lay the groundwork for future studies of flux variability in similar systems.

- **keywords**: Binary stars, astrometry, stars:formation — stars:kinematics

- **Article Reference:** The complete article, detailing the methods and results of this study, can be accessed at the following link: arXiv:2503.04594v1.

Chapter 5

Dynamical Mass of the EC 95 Multiple System

Continuing the estimation of dynamical masses in young stellar systems, this chapter presents a detailed analysis of EC 95, a hierarchical triple system located in the Serpens star-forming region (see Section §1.2). EC 95 consists of the close binary EC 95A and EC 95B, and a more distant tertiary component, EC 95C. Initially, EC 95 was classified as a proto-Herbig Ae/Be star based on photometric and spectroscopic observations (Preibisch, 1999). Subsequent VLBA observations revealed that the system comprises two compact components with an approximate separation of 15 mas (Dzib et al., 2010). Additional observations by Ortiz-León et al. (2017a) indicated that the primary and secondary components have similar masses of approximately 2 $M_{\odot}$ and identified EC 95C as a third component located $\sim$ 145 mas northeast of the binary barycenter, classifying the system as a hierarchical triple.

For this study, we analyzed 32 epochs of VLBA observations spanning 12 years. The dataset combines archival observations from projects BL155, BL160 (P.I.: L. Loinard), and BD155 (P.I.: S. Dzib), nine additional epochs from the GOBELINS survey (Ortiz-León et al., 2017a), and seven recent observations from the DYNAMO-VLBA project. The components were conclusively detected in all seven recent VLBA observations, as illustrated in Figure 5.1. Data calibration was performed using AIPS (Greisen, 2003), as described in earlier chapters. In total, EC 95A was detected in 30 epochs, and EC 95B in 23 epochs, as detailed in Table 5.1.

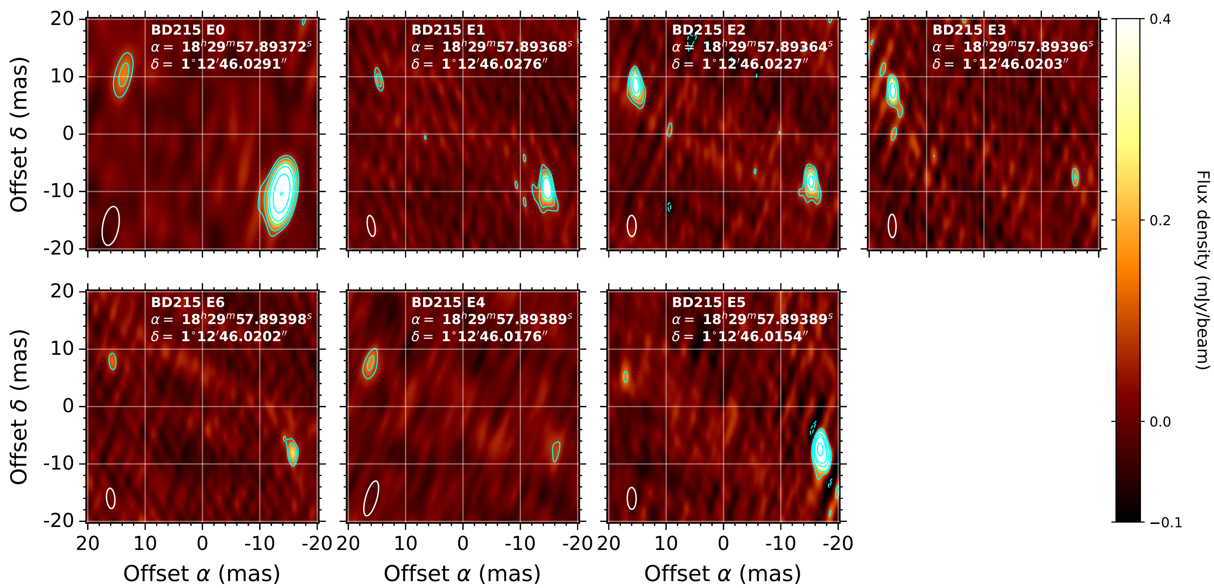

Figure 5.1: VLBA radio images of EC 95A and EC 95B at 4.9 GHz corresponding to each epoch observed during the DYNAMO-VLBA project. Intensity background images are clipped to intensities between –0.1 to 0.4 mJy beam^{-1}. Contour levels correspond to –3, 3, 6, 10, 15, 30, and 60 times the noise levels of the images, as detailed in Table 5.1. Each image is centered at the mid-point between EC 95A and EC 95B at the coordinates indicated in the top-left corner of each plot. The synthesized beam is represented by the white ellipse in the bottom-right corner of each plot.

The tertiary component, EC 95C, was detected in four epochs, and its measured properties are provided in Table 5.2. Figure 5.2 shows the VLBA image corresponding to project BD215E1, where all three components of EC 95 are detected.

Project name	Date UT (yyyy.mm.dd)	Date Julian Day	EC 95A α(J2000.0) 18^h29^m [^{s}]	EC 95A δ (J2000.0) $1°12'$ [$''$]	EC 95A $S_\nu \pm \sigma_{s_\nu}$ (mJy)	EC 95B α(J2000.0) 18^h29^m [^{s}]	EC 95B δ (J2000.0) $1°12'$ [$''$]	EC 95B $S_\nu \pm \sigma_{s_\nu}$ (mJy)	$\sigma_{\rm noise}$ (μJy bm^{-1})
BL156	2007.12.22	2454457.32	57.8909599(13)	46.107905(36)	1.79 ± 0.10	...	...	...	50
BL160A	2008.06.29	2454646.82	57.8909585(48)	46.107242(186)	0.47 ± 0.16	...	...	...	90
BL160B	2008.09.15	2454724.61	57.8908095(8)	46.105900(29)	4.51 ± 0.23	...	...	...	110
BL160C	2008.11.29	2454800.40	57.8908841(22)	46.104416(89)	1.03 ± 0.08	57.8918664(18)	46.110101(69)	1.24 ± 0.08	80
BL160D	2009.02.27	2454890.14	57.8911210(39)	46.103859(138)	0.41 ± 0.16	57.8921732(5)	46.106940(18)	4.01 ± 0.15	80
BL160E	2009.06.03	2454985.89	57.8910697(41)	46.104177(240)	1.57 ± 0.24	...	...	...	110
BL160F	2009.08.31	2455074.65	57.8909119(8)	46.103134(32)	3.11 ± 0.14	...	...	...	70
BL160G	2009.12.05	2455171.38	...	...	...	57.8922233(10)	46.095333(41)	2.77 ± 0.16	90
BL160H	2010.03.12	2455268.12	57.8913181(40)	46.100962(162)	0.18 ± 0.06	57.8924800(20)	46.092081(67)	0.60 ± 0.07	62
BL160I	2010.06.09	2455356.88	57.8912856(36)	46.101013(176)	0.77 ± 0.19	57.8924296(12)	46.089683(54)	1.72 ± 0.16	74
BL160J	2010.09.03	2455442.64	57.8911673(47)	46.099877(202)	0.32 ± 0.10	...	...	...	57
BD155A	2012.01.09	2455936.29	57.8918555(61)	46.091786(156)	0.39 ± 0.09	57.8925187(46)	46.068868(150)	0.56 ± 0.10	49
BD155B	2012.01.10	2455937.29	...	...	...	57.8925323(30)	46.068531(82)	0.54 ± 0.07	41
BD155C	2013.08.18	2456522.69	57.8924695(6)	46.081657(23)	1.37 ± 0.05	57.8923984(10)	46.053528(34)	0.91 ± 0.05	26
BD155D	2013.08.20	2456524.68	57.8924686(42)	46.081514(137)	0.22 ± 0.05	57.8923894(23)	46.053868(110)	0.38 ± 0.05	22
BL175E2	2013.09.03	2456538.71	57.8924432(69)	46.081859(229)	0.40 ± 0.06	57.8923300(15)	46.054528(49)	0.79 ± 0.05	28
BL175G1	2014.03.03	2456720.21	57.8929540(65)	46.078949(167)	0.24 ± 0.05	57.8926328(33)	46.049701(92)	0.69 ± 0.05	27
BL175CS	2014.10.13	2456943.60	57.8929236(38)	46.072521(108)	0.34 ± 0.04	57.8923327(53)	46.043694(190)	0.26 ± 0.05	26
BL175FE	2015.03.02	2457084.21	57.8933976(18)	46.068654(71)	1.04 ± 0.06	...	...	...	36
BL175GX	2015.10.07	2457302.61	57.8933947(77)	46.063120(262)	0.16 ± 0.04	...	...	...	25
BD155E	2016.01.03	2457391.31	57.8936486(1)	46.060099(6)	5.24 ± 0.05	...	...	...	25
BL175F8	2016.04.28	2457507.03	57.8938947(11)	46.058656(36)	1.17 ± 0.04	57.8926602(10)	46.032795(36)	1.18 ± 0.04	24
BL175IM	2016.09.09	2457640.67	57.8937768(10)	46.054508(34)	1.26 ± 0.04	57.8924047(7)	46.029802(25)	1.67 ± 0.04	19
BL175JF	2017.03.25	2457838.12	57.8943146(30)	46.048712(108)	0.26 ± 0.03	57.8927517(13)	46.025664(45)	0.66 ± 0.03	15
BL175KB	2017.09.16	2458012.65	57.8942206(57)	46.043325(181)	0.40 ± 0.03	57.8924793(40)	46.022171(130)	0.58 ± 0.03	20
BD215 E0	2018.02.24	2458174.10	57.8946426(141)	46.039506(498)	0.17 ± 0.04	57.8928053(13)	46.018779(43)	1.41 ± 0.04	24
BD215 E1	2018.06.28	2458297.76	57.8946522(59)	46.037134(231)	0.13 ± 0.03	57.8927006(15)	46.018150(56)	0.77 ± 0.04	21
BD215 E2	2018.11.04	2458427.41	57.8946539(21)	46.031121(77)	0.64 ± 0.05	57.8926166(25)	46.014326(88)	0.56 ± 0.05	26
BD215 E3	2019.03.04	2458547.09	57.8950226(28)	46.027755(115)	0.52 ± 0.06	57.8929021(55)	46.012754(240)	0.14 ± 0.04	36
BD215 E6	2019.03.07	2458550.07	57.8950243(95)	46.028162(322)	0.14 ± 0.05	57.8929306(46)	46.012200(171)	0.26 ± 0.04	28
BD215 E4	2019.07.12	2458676.73	57.8949590(120)	46.024994(356)	0.16 ± 0.04	57.8928162(183)	46.010285(706)	0.13 ± 0.05	27
BD215 E5	2019.11.09	2458797.40	57.8950192(92)	46.020537(365)	0.20 ± 0.06	57.8927570(9)	46.007717(30)	1.98 ± 0.06	45

Table 5.1: EC 95A and EC 95B measured positions and flux densities for the 32 VLBA observations.

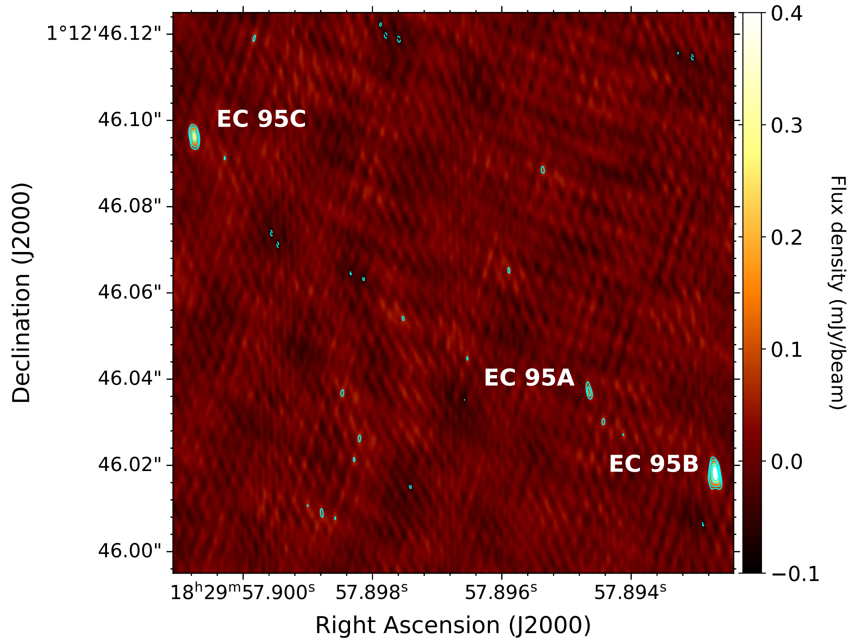

Figure 5.2: VLBA radio image of EC 95 at 4.9 GHz for epoch BD215E1, showcasing the detection of all three components (EC 95A, EC 95B, and EC 95C) in the system. The contour levels are as in Fig. 5.1.

Project name	Date UT (yyyy.mm.dd)	Date Julian Day	EC 95C α(J2000.0) 18^h29^m [^{s}]	δ (J2000.0) $1^\circ 12'$ [$''$]	$S_\nu \pm \sigma_{s_\nu}$ (mJy)	ρ[a] (mas)	PA[a] (°)
BL160B	2008.09.15	2454724.61	57.8985675(3)	46.205651(108)	0.86 ± 0.19	145.93±0.08	48.87±0.04
BD155A	2012.01.09	2455936.29	57.8994536(6)	46.166823(19)	0.56 ± 0.10	138.81±0.08	51.64±0.04
BL175KB	2017.09.16	2458012.65	57.9004380(10)	46.103750(30)	2.28 ± 0.03	127.24±0.08	56.64±0.05
BD215 E1	2018.06.28	2458297.76	57.9007544(136)	46.096234(606)	0.30 ± 0.03	126.04±0.38	57.25±0.25
VLT obs.[b]	2005.05.22	2453512.85	...	...	...	152±1	47.2±0.5

[a] The separation (ρ) and position angle (PA; North through East) are taken with respect to the barycenter (VLBA) or the photocenter (IR) of the close binary EC 95AB.
[b] Reference: Duchêne et al. (2007).

Table 5.2: EC 95C measured positions and flux densities.

5.0.1 Determination of the Dynamical Masses of the Primary and Secondary Components in the EC 95 System

To determine the orbital and astrometric parameters of EC 95, we fitted the positions of EC 95A and EC 95B using MPFIT (Kounkel et al., 2017), yielding individual dynamical mass estimates of 2.15 ± 0.10 $M_\odot$ for EC 95A and 2.00 ± 0.12 $M_\odot$ for EC 95B. The results of the best fit are presented in Table 5.3, while the visualizations of the total sky motion and orbital motion are shown in Figures 5.3 and 5.4, respectively. To compare the accuracy of the orbital parameters derived from the least-squares fit, we employed the *Orbitize!* package (Blunt et al., 2017). Prior distributions for the orbital elements were established, and the MCMC analysis was performed using 10,000 walkers and 10,000 iterations. The final results are summarized in Table 5.4, while Figure 5.10 in Appendix 5.0.4 displays the posterior distributions of the fitted parameters. Additionally, Figure 5.5 presents 2,000 orbital solutions that fit the observational data, obtained through the MCMC exploration. The estimated total mass of the close binary system is 4.52 $^{+0.25}_{-0.23}$ M⊙, which is consistent within 1σ with the mass derived using MPFIT.

Parameter	Value	Units
Astrometric parameters		
$\alpha_{2016.0,\mathrm{centre}}$	18:29:57.8931008(53)	hh:mm:ss
$\delta_{2016.0,\mathrm{centre}}$	1:12:46.048129(117)	° : ′ : ″
μ_α	3.54 ± 0.02	mas yr^{-1}
μ_δ	−8.42 ± 0.02	mas yr^{-1}
π	2.30 ± 0.04	mas
d	435.71 ± 7.43	pc
Orbital parameters		
a_1	6.00 ± 0.15	AU
a_2	6.46 ± 0.09	AU
$a = a_1 + a_2$	12.46 ± 0.18	AU
P	21.61 ± 0.11	years
T_0	2454779.43 ± 33.00	Julian date
e	0.391 ± 0.003	
Ω	305.56 ± 1.13	degrees
i	30.44 ± 0.26	degrees
ω	117.27 ± 0.51	degrees
Dynamical masses		
M_{A+B}	4.146 ± 0.212	M$_\odot$
M_A	2.148 ± 0.097	M$_\odot$
M_B	1.998 ± 0.116	M$_\odot$

Table 5.3: Best-fit model parameters for the close binary system EC 95AB using MPFIT.

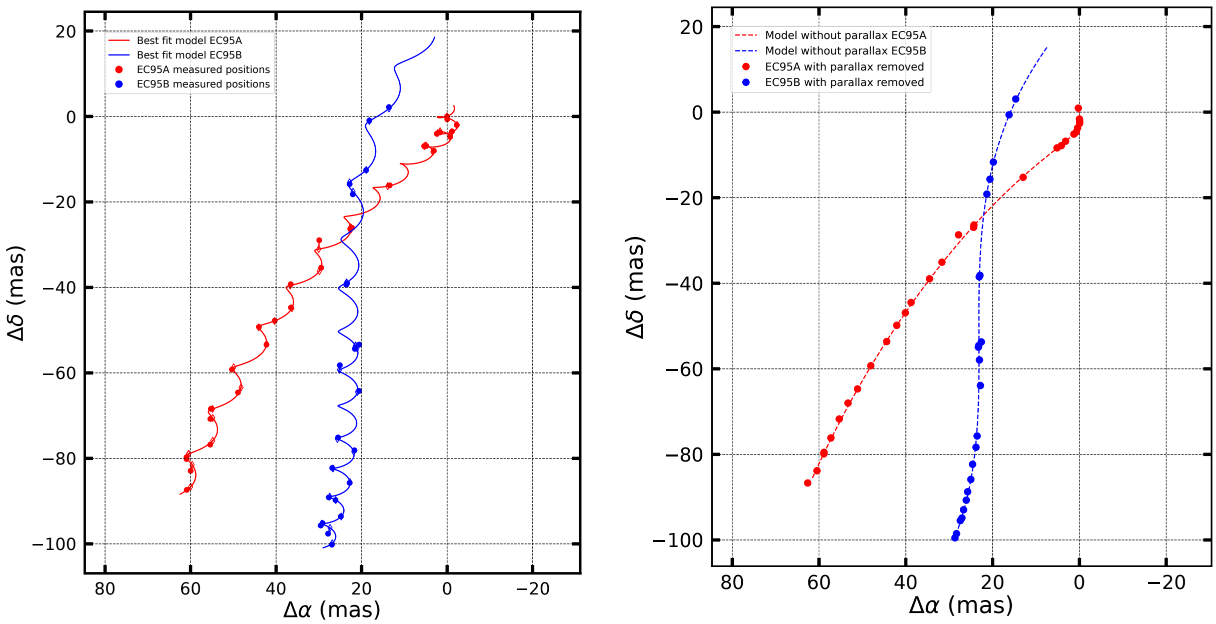

Figure 5.3: Measured positions of EC 95A (red dots) and EC 95B (blue dots) shown as offsets from the position of EC 95A in the first detected epoch in VLBA observations (2007 December 22, see Table 5.1). Left: The blue and red curves show the best-fit stellar motions, as described in the text, for EC 95A and EC 95B, respectively. Right: The measured positions and best fit after removing the parallax signature.

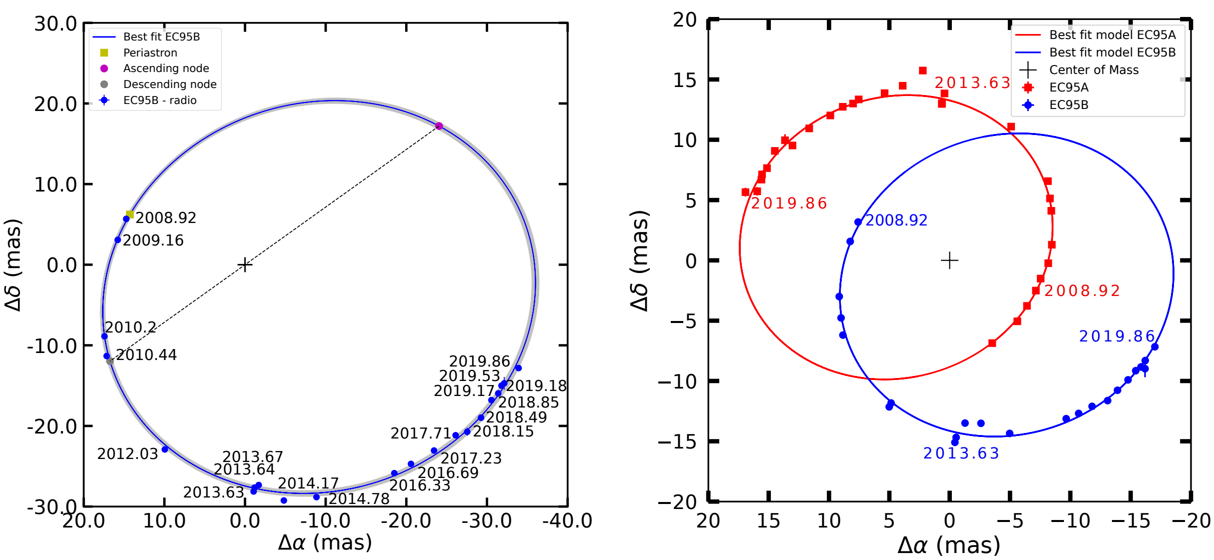

Figure 5.4: Left: Relative positions and orbital fit model for EC 95AB. The blue dots indicate the relative positions of EC 95B with respect to EC 95A, and the error bars consider the position errors of both components added in quadrature. The dashed black line traces the line of nodes from the model, and the black cross indicates the position of the primary source. Right: Stellar orbits for EC 95AB are shown relative to the center of mass (black cross).

Parameter	Value	Units
Orbital Parameters		
a	$13.51^{+0.26}_{-0.24}$	AU
e	$0.393^{+0.002}_{-0.002}$	
Ω	317.21 ± 0.82	degrees
i	$35.44^{+0.34}_{-0.33}$	degrees
ω	115.91 ± 0.38	degrees
T_0	2458862.0 ± 0.25	Julian date
P	23.37 ± 0.22	years
M_{A+B}	$4.52^{+0.25}_{-0.23}$	$M_\odot$

Table 5.4: Best-fit model parameters for the close binary system EC 95AB using *Orbitize!* The values of ω and Ω refer to EC 95B.

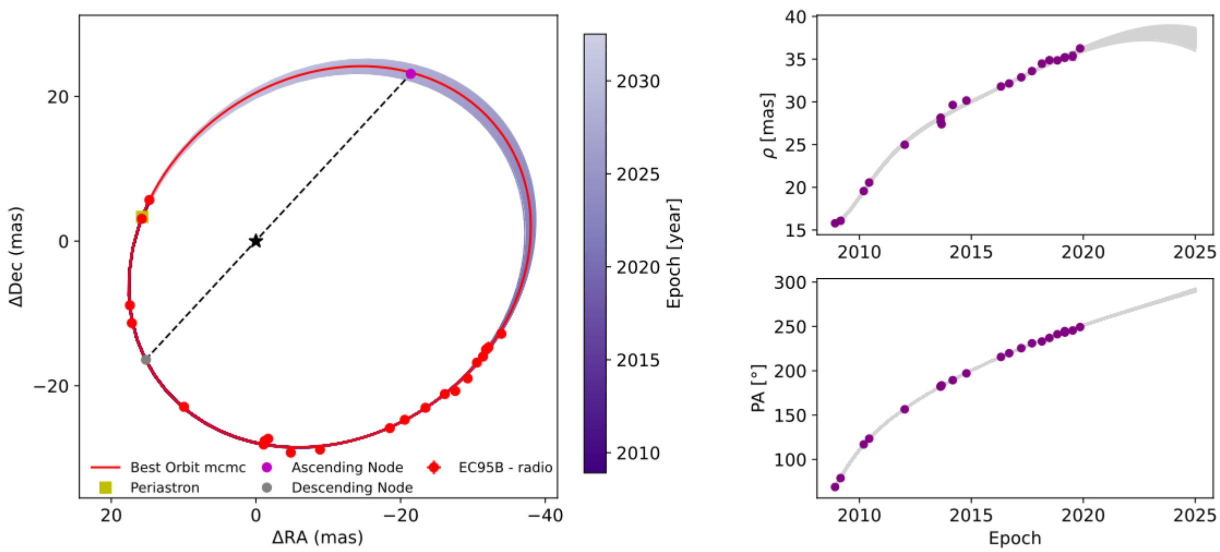

Figure 5.5: Allowed orbital configurations for the close binary EC 95AB derived from the MCMC analysis conducted using the *Orbitize!* package. The red orbit corresponds to the best-fit orbit from the MCMC analysis. The black marker (star) designates the position of the primary component. The color bar indicates time measured from the first observation. The upper right panel depicts the evolution of the angular separation over time, while the lower right panel illustrates the variation in the position angle throughout the orbits.

5.0.2 Estimating the Mass of the Third Component in the EC 95 System

The mass of EC 95C was estimated by modeling the hierarchical system as a central binary with EC 95C orbiting its center of mass. Four VLBA detections, along with a VLT infrared observation (Duchêne et al., 2007), provided measurements of the orbital separation and position

Parameter	Value	Units
Orbital Parameters		
a	$52.19\,^{+2.01}_{-2.17}$	AU
e	0.75 ± 0.03	
Ω	$169.23^{+7.71}_{-12.44}$	degrees
i	$37.22^{+3.15}_{-5.26}$	degrees
ω	$43.49^{+11.03}_{-7.34}$	degrees
T_0	$2458881.90\,^{+2.99}_{-3.33}$	Julian date
P	$172.30\,^{+13.45}_{-13.82}$	years
M_{A+B+C}	$4.76\,^{+0.45}_{-0.36}$	$M_{\odot}$

Table 5.5: Best-fit model parameters for EC 95C using *Orbitize!*

angle of EC 95C relative to the binary. The corresponding separations and position angles are given in Table 5.2. Using the *Orbitize!* package, which provides only the total system mass, we estimated the combined mass of components A+B+C to be $4.76^{+0.45}_{-0.36}\,M_{\odot}$. Subtracting the previously determined masses of EC 95A and EC 95B yielded an estimate for the mass of EC 95C of $0.26^{+0.53}_{-0.46}\,M_{\odot}$. The parameters estimated from this analysis are presented in Table 5.5. Figure 5.6 shows the orbits derived from 2,000 MCMC samples, while the posterior corner plot is provided in Figure 5.11 in Appendix 5.0.4.

These results suggest that EC 95C is a low-mass T Tauri star, marking the first time its mass has been estimated. The uncertainty in the mass of EC 95C arises from the statistical nature of its determination. Unlike EC 95A and EC 95B, whose masses are directly constrained by orbital fitting, the mass of EC 95C is inferred by difference, subtracting their values from the total system mass. Limited orbital coverage weakens these constraints, leading to a posterior distribution with significant dispersion, broadening the range of possible values and, in some cases, allowing solutions that include unphysical (i.e., negative) values. Additionally, MCMC methods, when applied to systems with sparse detections, can produce large uncertainties and biases in parameter distributions. These limitations reflect the lack of observational information rather than a physical inconsistency, highlighting the need for future observations to reduce the uncertainty in the mass estimation of EC 95C.

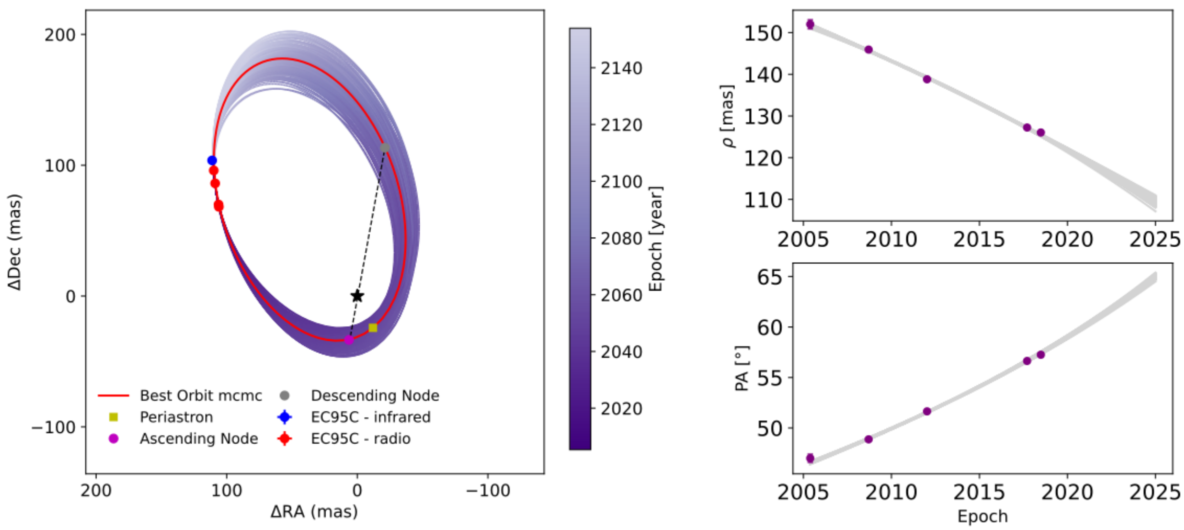

Figure 5.6: Allowed orbital configurations for component EC 95C, derived from MCMC analysis using *Orbitize!*. The blue point corresponds to the near-infrared (NIR) detection obtained at the VLT in 2005 (Duchêne et al., 2007), while the red points represent radio detections detailed in Table 5.2. The red orbit corresponds to the best-fit orbit from the MCMC analysis. The color bar indicates time measured from the first observation. The upper right panel shows angular separation, and the lower right panel displays position angle variation during orbit.

5.0.3 Pre-Main Sequence Evolution Models and the SED of EC 95

To compare the dynamical masses with theoretical predictions, we analyzed the SED of EC 95 using photometric data from VizieR. Assuming an effective temperature of $4,400\,K$ (Preibisch, 1999; Doppmann et al., 2005), we derived a total luminosity of $241 \pm 20\,L_\odot$ and an extinction of $A_V = 34.2 \pm 2.5$ mag, as shown by the blue curve in Figure 5.7. In addition to the reddened blackbody model, we performed an SED fit based on the SEDFit package. We used the same parameters as in the reddened blackbody analysis, fixing both the temperature and stellar radius. The results from this fit show good agreement with the photometric data, as shown by the red curve in Figure 5.7. Given that the SED analysis accounts for the contribution of both stars in the system, and because the components have comparable masses, we assume that both stars have similar luminosities of 120 ± 10 L$_\odot$, which corresponds to a radius of 18.9 ± 0.8 R$_\odot$. With these parameters, the stars were positioned within the pre-main sequence stellar evolution models (see Section §1.5). Comparisons with models including BaSTI (Pietrinferni et al., 2004, 2006), YaPSI (Spada et al., 2017), MIST-MESA (Paxton et al., 2011; Choi et al., 2016), and PARSEC

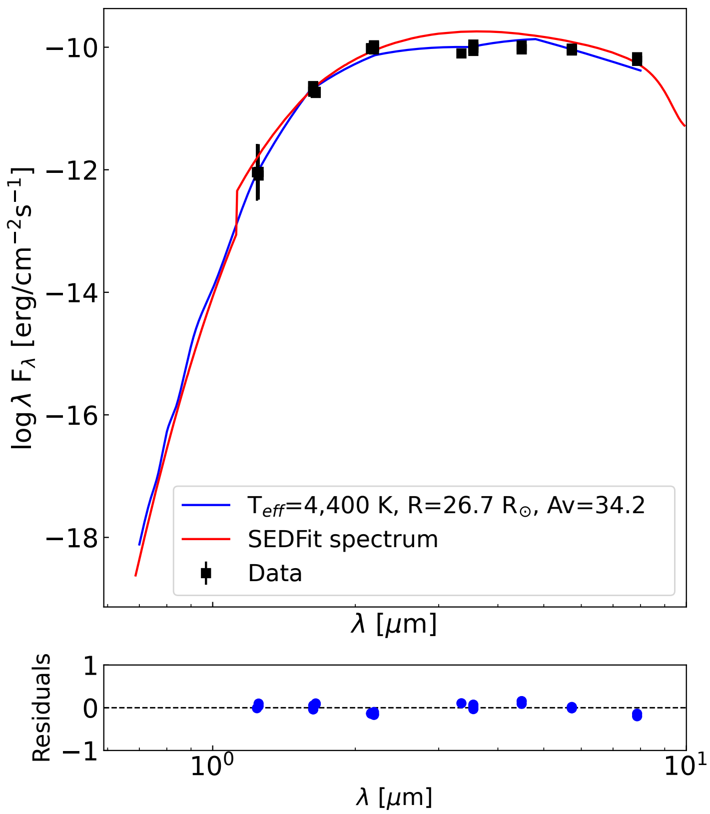

Figure 5.7: Spectral energy distribution of EC 95. The data points (black squares) are taken from VizieR. The blue curve represents the SED fit with a blackbody using extinction models from Fitzpatrick et al. (2019) and Rieke et al. (1989), while the red curve corresponds to the SED fit to the spectrum using the SEDFit package. The figure also includes residual plot for the reddened blackbody model (bottom panel).

V2.0 (Nguyen et al., 2022), confirm a mass of 2 $M_\odot$ for EC 95A and EC 95B at very young ages (between 5×10^3 and 1×10^4 years). In contrast, the models of Siess et al. (2000) overestimated the masses, suggesting values of 3.5–4 $M_\odot$, inconsistent with the dynamical results and yielding ages between 2.2×10^4 and 9.3×10^4 years. The corresponding evolutionary tracks for each model are shown in Figure 5.8.

These results confirm that the central binary system EC 95AB consists of two young stars, each with a mass of approximately 2, $M_\odot$. Previous estimates by Preibisch (1999), which assumed EC 95 to be a single star, calculated a mass of ~4 $M_\odot$ based on a historically shorter distance (310 pc) estimated for the Serpens region. Our updated distance of 435.71 ± 7.43 pc, combined with the determination of the system luminosity, provides a clearer and more accurate understanding of the components of the close binary.

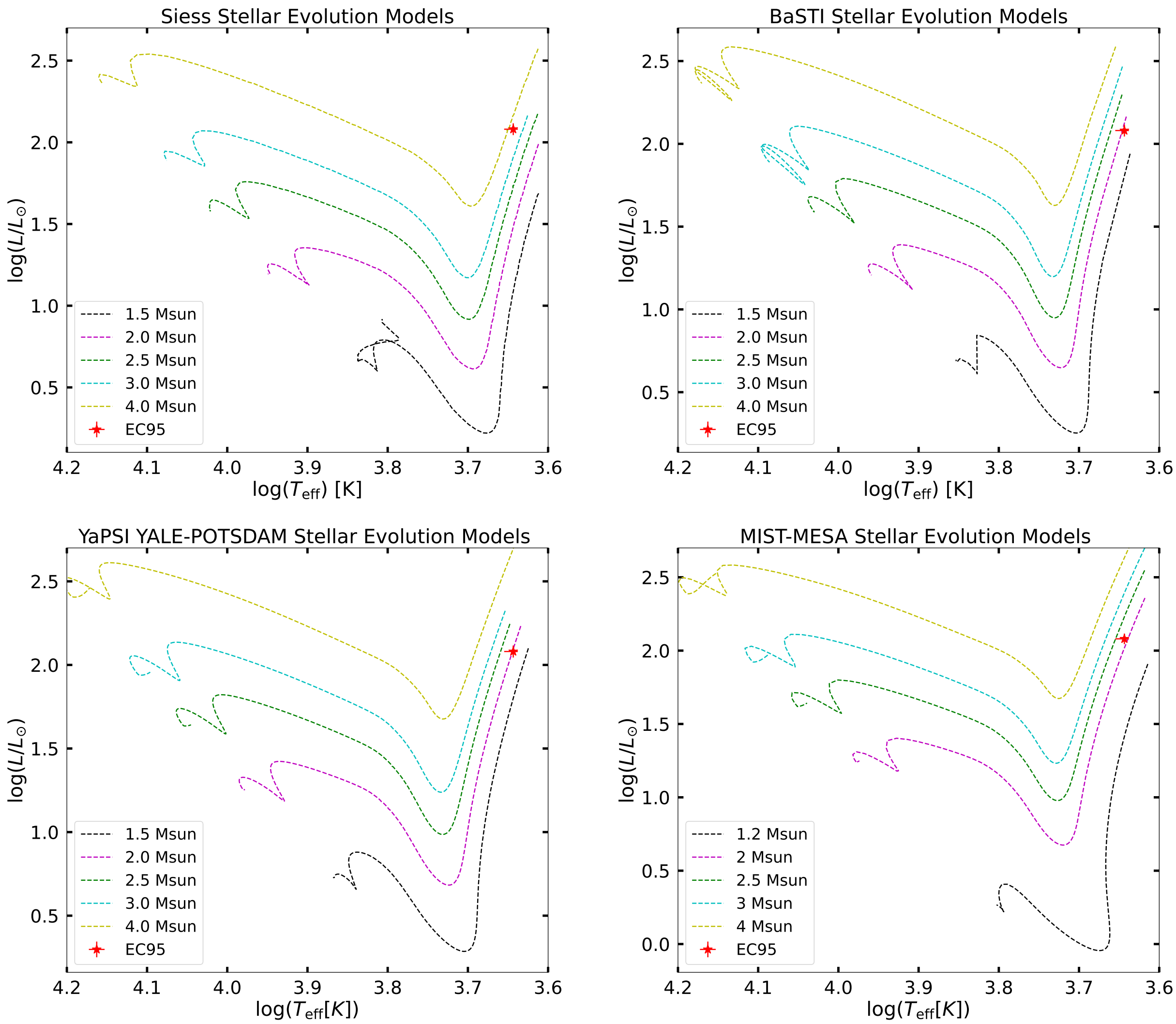

Figure 5.8: Location of EC 95 on the HR diagram and evolutionary tracks based on pre-main sequence stellar evolution models. Top left: Siess et al. (2000) models. Top right: BaSTI models (Pietrinferni et al., 2004, 2006). Bottom left: YaPSI YALE-POTSDAM models by Spada et al. (2017). Bottom right: MIST-MESA models (Paxton et al., 2011; Choi et al., 2016). These models assume a metallicity $Z = 0.02$, helium abundance $Y = 0.2880$, mixing-length parameter $\alpha = 1.90$, and deuterium abundance $X_D = 4 \times 10^{-5}$. The red star marks the predicted location of EC 95 with $T_{\rm eff} = 4,400^{+115}_{-57}$ K and $L = 120 \pm 10$ $L_\odot$.

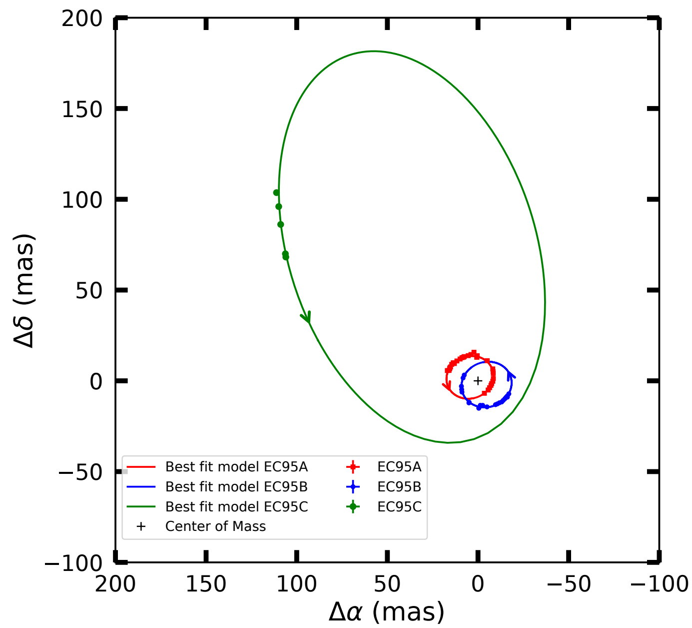

Figure 5.9: Orbits of EC 95A (red line), EC 95B (blue line) and EC 95C (green line) around the center of mass of the system (black cross). The colored squares indicate the measured positions, while the arrows show the direction of the orbits.

Finally, the dynamical mass estimate of 0.26 $M_\odot$ for EC 95C establishes it as the least massive member of the system and further confirms its classification as a young low-mass T Tauri star. Additionally, the orbital modeling of the three components of EC 95 reveals a hierarchical configuration, where EC 95C orbits the center of mass of the tight binary EC 95AB, as illustrated in Figure 5.9, which displays the three orbital trajectories within the system. The inclination angles of the orbits of EC 95AB and EC 95C are similar (approximately 35°), consistent with a formation scenario involving disk fragmentation (Adams et al., 1989). However, the orbits exhibit significant eccentricity and a notable misalignment in the orientation of their semi-major axes, as indicated by the values of ω and Ω. Near periastron, the separation between EC 95C and the AB barycenter (11.77 AU) becomes comparable to the separation between the binary components themselves, raising important questions about the long-term stability of the system. Such configurations are often susceptible to dynamical interactions, which could lead to instability over time. To better constrain the orbital parameters of EC 95C and evaluate the stability of the system, continued VLBI observations and complementary infrared monitoring will be critical in the coming decades.

5.0.4 Appendix: MCMC Corner Plots for the EC 95 System

This appendix presents the corner plots obtained from the MCMC analysis conducted with the *Orbitize!* package for the EC 95AB and EC 95C components of the triple system. These plots illustrate the posterior distributions of the orbital parameters derived from the MCMC exploration.

For EC 95A, the analysis was based on 23 epochs in which both components were simultaneously detected. In the case of EC 95C, five detections were considered (4 VLBA + 1 VLT). The position of EC 95C was measured relative to the barycenter of EC 95AB, which was determined for each epoch using the astrometric results derived from the VLBA observations and modeled with MPFIT. Figures 5.10 and 5.11 show the resulting posterior distributions for EC 95AB and EC 95C, respectively.

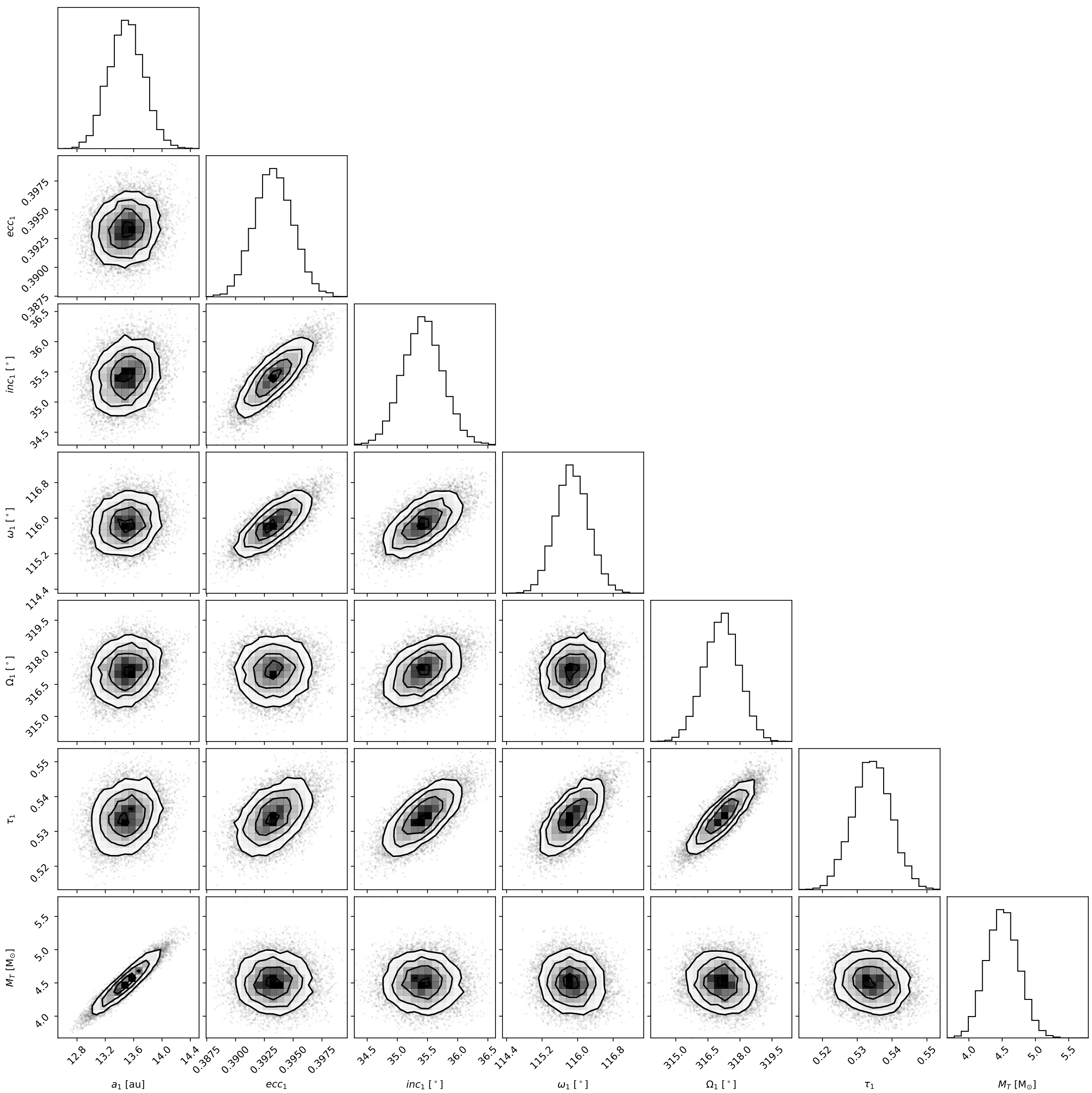

Figure 5.10: Posterior corner plot from the MCMC analysis of the close binary EC 95AB using the *Orbitize!* package. The diagonal panels show the 1D marginalized posterior distributions for the orbital parameters: semi-major axis (a), eccentricity (e), inclination (i), argument of periastron (ω), longitude of the ascending node (Ω), time of periastron passage (τ), and total system mass. The off-diagonal panels display the correlations between these parameters.

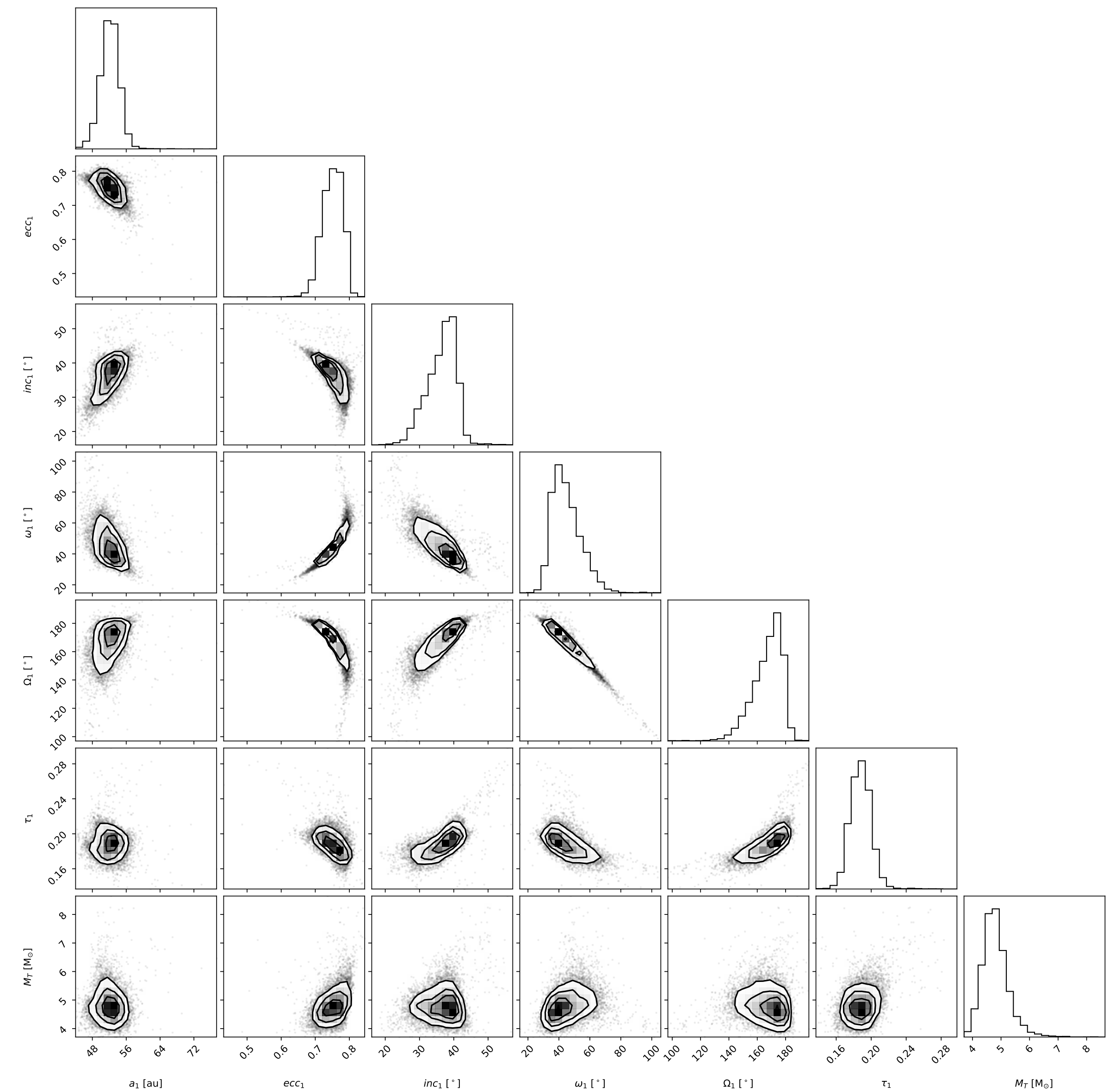

Figure 5.11: Posterior corner plot from the MCMC analysis of the total mass of the EC 95 triple system using *Orbitize!*. The diagonal panels show the 1D posterior distributions for each orbital parameter, while the off-diagonal panels illustrate the covariances between them.

Chapter 6

Summary and Conclusions

In this thesis, the importance of accurately measuring stellar mass has been emphasized, given that it is a fundamental parameter in the life of a star, determining its luminosity, internal structure, energy source, lifetime, and ultimate fate. Accurate mass measurements are crucial to validate and improve theoretical models of stellar evolution. In this context, multiple and binary systems are key tools for this purpose, allowing for the direct determination of stellar masses through the analysis of orbital parameters and Kepler laws. In particular, it has also been highlighted that young binary systems provide a unique window into the study of stars during their early evolutionary stages. These stars, typically embedded in dense regions of gas and dust, present significant observational challenges; however, the data obtained from such systems are essential for refining pre-main sequence theoretical models. The challenge is especially significant in tight binary systems, which exhibit extremely small angular separations on the order of milliarcseconds. Their study is further complicated at optical and infrared wavelengths, as the opacity of the interstellar medium blocks most of the radiation emitted by these systems. Astrometric missions like Gaia, although highly successful at resolving wider systems, lack the capability to address such narrow separations or penetrate the dense star-forming regions where these systems are located.

To overcome these limitations, this thesis focused on observations conducted using VLBI, a method that combines signals from multiple radio telescopes separated by thousands of kilometers. This approach enables unprecedented angular resolution and astrometric precision.

Unlike other techniques, VLBI does not rely on internal field references but instead anchors its measurements to the *International Celestial Reference Frame* (ICRF), defined by distant extragalactic quasars. These quasars, considered fixed points on the celestial sphere due to their apparent immobility, provide a globally stable and highly precise reference frame. This capability allows VLBI to measure absolute positions with microarcsecond precision, which is fundamental for deriving orbital parameters and dynamical masses of individual components without relying on additional assumptions about luminosity or spectral type.

Through VLBI observations, primarily obtained from the DYNAMO-VLBA project, the dynamical masses of the intermediate-mass young stellar systems S1 in Ophiuchus and EC 95 in Serpens were determined. For the S1 system, the primary star, S1A, was determined to have a mass of 4.115 ± 0.039 $M_\odot$, significantly lower than previous estimates based on stellar evolution models, which suggested a mass of 5–6 $M_\odot$. This finding demonstrates that current stellar evolution models overestimate the mass of this intermediate-mass pre-main sequence star by 20 to 50%, highlighting the need for adjustments and refinements to these models. Additionally, the secondary star, S1B, was confirmed to have a mass of $0.814 \pm 0.006\ M_\odot$, and the hypothesis that the lack of detection near periastron was due to optically thick regions was ruled out. Furthermore, a comparison of VLBI results with Gaia measurements revealed that the Gaia position does not exactly match the VLBI-measured position of S1A, as expected, since Gaia observes the motion of the system photocenter, predominantly influenced by the primary star. Gaia cannot resolve the system orbit or measure its parallax with the same precision and reliability.

For the triple system EC 95, VLBI yielded highly precise measurements of the dynamical masses of the primary components: EC 95A ($2.15 \pm 0.10\ M_\odot$) and EC 95B ($2.00 \pm 0.12\ M_\odot$), and provided the first-ever mass estimate for the tertiary component, EC 95C ($0.26^{+0.53}_{-0.46}\ M_\odot$). These results align well with theoretical models for masses around 2, $M_\odot$ for EC 95AB, including BaSTI (Pietrinferni et al., 2004, 2006), YaPSI (Spada et al., 2017), MIST-MESA (Paxton et al., 2011; Choi et al., 2016), and PARSEC V2.0 (Nguyen et al., 2022)—suggesting that predictions in this regime are generally reliable. In contrast, the models of Siess et al. (2000) significantly overestimate the masses, highlighting a notable discrepancy with the dynamical results.

The results presented in this thesis highlight the unique capabilities of VLBI for studying young stellar systems, particularly in resolving tight binaries and determining dynamical masses with high precision. While VLBI remains indispensable for such studies, the development of next-generation instruments will offer complementary capabilities that significantly expand our understanding of these objects. Among these advancements, the *Next Generation Very Large Array* (ngVLA)[1] is designed to achieve a sensitivity ten times greater than that of the current VLA, enabling the detection of weaker thermal and non-thermal emissions from young stellar objects (YSOs) at milli-arcsecond scales. This increased sensitivity will be critical for detailed studies of circumstellar disks, jets, and faint companions in dense star-forming regions, providing a more comprehensive view of the environments surrounding these systems. Similarly, the *Square Kilometre Array* (SKA)[2] will allow for the exploration of large areas of the sky, offering an unprecedented perspective on stellar populations across various star-forming regions. This instrument will facilitate the study of extended structures and large-scale properties of stellar environments. Additionally, infrared astrometry missions such as the *Japan Astrometry Satellite Mission for Infrared Exploration* (JASMINE)[3] will provide a unique perspective by focusing on highly obscured regions of the Galactic bulge and disk. By operating in the infrared range, JASMINE will enable the study of stellar populations and embedded objects that are not observable in optical wavelengths, thus broadening our understanding of star formation in dusty and dense environments. These next-generation instruments, with their complementary capabilities, will provide an integrated framework for advancing the study of young stellar systems and refining theoretical models of stellar evolution across a wide range of environments and masses.

However, it is important to emphasize that, despite the emergence of these next-generation instruments, which will undoubtedly serve as complementary tools, VLBI remains an indispensable method for studying systems like those analyzed in this thesis. Its unique advantages, including unmatched angular resolution and astrometric precision, among others already mentioned, continue to position it as a leading technique in this field.

[1] https://ngvla.nrao.edu/
[2] https://www.skatelescope.org/
[3] https://jasmine.nao.ac.jp/

6.1 Future Work

Based on the results obtained in this thesis, a natural next step is to apply the same astrometric and orbital analysis methodology to other DYNAMO-VLBA sources that have not yet been thoroughly examined. Table 6.1 presents a list of additional binary systems located in various star-forming regions such as Ophiuchus, Serpens, Orion and Taurus. These systems span a broad range of spectral types (approximately F7–M5) and include both Class II and III objects. Determining the dynamical masses of these additional targets will provide a more extensive dataset, enabling direct comparisons between the intrinsic physical properties of young stars and the predictions of pre-main sequence evolutionary models. This expanded sample is essential for identifying general trends and testing observational results against theoretical expectations.

Additionally, continuous VLBA monitoring of systems like EC 95 is essential to refine orbital parameters and evaluate long-term dynamical stability. As demonstrated in this study, the hierarchical configuration and close periastron separations raise critical questions about their evolution and stability. Improved orbital coverage will enable tighter constraints on key parameters and help address remaining uncertainties in current models. To this end, we have submitted a VLBA observing proposal to continue monitoring the EC 95 system. This VLBA program aims to observe the system twice per year during the solstices from 2025 to 2028, providing a more complete phase coverage that will enhance constraints on the tertiary component orbit and further refine its mass estimation.

In summary, future work will focus on increasing the number of systems with directly measured dynamical masses and systematically comparing these results to evolutionary models. Through this effort, we aim to refine our understanding of the early formation and evolution of multiple stellar systems.

Name	Right Ascension (J2000.0)	Declination (J2000.0)	IR Class	Spectral Type	Period (years)
Ophiuchus					
WLY 2-11	$16^h25^m56.^s09$	$-24°30'15.''3$	III	M5	~ 4.5
LFAM 15	$16^h26^m42.^s44$	$-24°26'26.''1$	III	...	3.59 ± 0.02
VSSG 11	$16^h26^m43.^s76$	$-24°16'33.''4$	III	M0	~ 10
LFAM 18	$16^h26^m49.^s23$	$-24°20'03.''3$	III	K6	...
YLW 12Bab	$16^h27^m18.^s17$	$-24°28'52.''9$	III	F7	1.425 ± 0.001
ROXN 39	$16^h27^m21.^s81$	$-24°43'35.''9$	III	M3	11.2 ± 1.5
SFAM 87	$16^h30^m35.^s63$	$-24°34'18.''9$	...	K5	7.69 ± 0.01
DoAr 51	$16^h32^m11.^s79$	$-24°40'21.''8$	II	M3	8.10 ± 0.06
Serpens					
GFM 65	$18^h30^m00.^s65$	$+01°13'40.''0$	III	M0.5	~ 2
Tauro					
V 1096 Tau	$4^h13^m27.^s23$	$+28°16'24.''4$	III	M0	~ 3
Hubble 4	$4^h18^m47.^s04$	$+28°20'07.''2$	III	K7	9.28 ± 0.01
V 1201 Tau	$4^h24^m48.^s16$	$+26°43'16.''1$	...	K1	9.1 ± 1.2
V 1000 Tau	$4^h42^m07.^s32$	$+25°23'03.''0$	III	M1	5.6 ± 0.11
Orión					
VLBA 5	$5^h35^m11.^s80$	$-05°21'49.''3$	...	K5	...
VLBA 6	$5^h35^m18.^s37$	$-05°22'37.''4$	III	K0	...
VLBA 27	$5^h35^m31.^s37$	$-05°16'02.''6$	...	...	1.33 ± 0.01
VLBA 58	$5^h41^m37.^s74$	$-01°53'51.''6$	III	G8	0.73 ± 0.01
VLBA 125	$5^h41^m38.^s24$	$-01°53'09.''2$	III	...	...
VLBA 4/107	$5^h35^m21.^s32$	$-05°12'12.''7$	III	G2	6.3 ± 0.5
VLBA 61/62	$5^h41^m46.^s16$	$-01°56'22.''2$	...	...	9.5 ± 0.7
VLBA 68	$5^h46^m43.^s39$	$+00°04'36.''0$	III	...	1.8 ± 0.1

Table 6.1: List of additional binary systems from the DYNAMO-VLBA project for future analysis.

References

Adams, F. C., Lada, C. J., & Shu, F. H. 1987, ApJ, 312, 788

Adams, F. C., Ruden, S. P., & Shu, F. H. 1989, ApJ, 347, 959

Alecian, E., Wade, G. A., Catala, C., et al. 2013, MNRAS, 429, 1027

Alexander, D. R. & Ferguson, J. W. 1994, ApJ, 437, 879

Andre, P., Montmerle, T., Feigelson, E. D., Stine, P. C., & Klein, K.-L. 1988, ApJ, 335, 940

Andre, P., Phillips, R. B., Lestrade, J.-F., & Klein, K.-L. 1991, ApJ, 376, 630

André, P., Ward-Thompson, D., & Barsony, M. 1993, ApJ, 406, 122

Angulo, C., Arnould, M., Rayet, M., et al. 1999, Nucl. Phys. A, 656, 3

Bailer-Jones, C. A. L. 2015, PASP, 127, 994

Blunt, S., Nielsen, E. L., De Rosa, R. J., et al. 2017, AJ, 153, 229

Blunt, S., Wang, J. J., Angelo, I., et al. 2020, AJ, 159, 89

Bonnell, I. A. & Bate, M. R. 1994, MNRAS, 271, 999

Brogan, ALMA Partnership, C. L., Pérez, L. M., et al. 2015, ApJ, 808, L3

Carroll, B. W. & Ostlie, D. A. 1996, An Introduction to Modern Astrophysics

Cassisi, S., Potekhin, A. Y., Pietrinferni, A., Catelan, M., & Salaris, M. 2007, ApJ, 661, 1094

Charlot, P., Jacobs, C. S., Gordon, D., et al. 2020, A&A, 644, A159

Choi, J., Dotter, A., Conroy, C., et al. 2016, ApJ, 823, 102

Clark, P. C., Glover, S. C. O., Smith, R. J., et al. 2011, Science, 331, 1040

Dauphas, N. & Chaussidon, M. 2011, Annual Review of Earth and Planetary Sciences, 39, 351

Dopita, M. A., Schwartz, R. D., & Evans, I. 1982, ApJ, 263, L73

Doppmann, G. W., Greene, T. P., Covey, K. R., & Lada, C. J. 2005, AJ, 130, 1145

Duchêne, G., Bontemps, S., Bouvier, J., et al. 2007, Astronomy and Astrophysics, 476, 229

Duchêne, G. & Kraus, A. 2013, ARA&A, 51, 269

Dudorov, A. E. & Eretnova, O. V. 2016, Astronomical and Astrophysical Transactions, 29, 437

Dulk, G. A. 1985, ARA&A, 23, 169

Dunham, M. M., Allen, L. E., Evans, Neal J., I., et al. 2015, ApJS, 220, 11

Duquennoy, A. & Mayor, M. 1991, A&A, 248, 485

Dzib, S., Loinard, L., Mioduszewski, A. J., et al. 2010, ApJ, 718, 610

Dzib, S., Loinard, L., Rodríguez, L. F., Mioduszewski, A. J., & Torres, R. M. 2011, Astrophysical Journal, 733, 71

Dzib, S. A., Ortiz-León, G. N., Loinard, L., et al. 2018, ApJ, 853, 99

Dzib, S. A., Ortiz-León, G. N., Loinard, L., et al. 2016, ApJ, 826, 201

Eiroa, C. & Casali, M. M. 1989, A&A, 223, L17

Eiroa, C., Djupvik, A. A., & Casali, M. M. 2008, The Serpens Molecular Cloud, ed. B. Reipurth, Vol. 5, 693

Eiroa, C., Torrelles, J. M., Curiel, S., & Djupvik, A. A. 2005, AJ, 130, 643

Eisner, J. A., Hillenbrand, L. A., Carpenter, J. M., & Wolf, S. 2005, ApJ, 635, 396

Estalella, R., Anglada, G., Rodríguez, L. F., & Garay, G. 1991, ApJ, 371, 626

Feigelson, E. D. & Montmerle, T. 1999, ARA&A, 37, 363

Felli, M., Taylor, G. B., Neckel, T., & Staude, H. J. 1998, A&A, 329, 243

Ferguson, J. W., Alexander, D. R., Allard, F., et al. 2005, ApJ, 623, 585

Fey, A. L., Gordon, D., Jacobs, C. S., et al. 2015, AJ, 150, 58

Fiorellino, E., Manara, C. F., Nisini, B., et al. 2021, A&A, 650, A43

Fisher, R. T. 2004, ApJ, 600, 769

Fitzpatrick, E. L. 1999, PASP, 111, 63

Fitzpatrick, E. L., Massa, D., Gordon, K. D., Bohlin, R., & Clayton, G. C. 2019, ApJ, 886, 108

Foreman-Mackey, D., Hogg, D. W., Lang, D., & Goodman, J. 2013, PASP, 125, 306

Galli, P. A. B., Loinard, L., Ortiz-Léon, G. N., et al. 2018, ApJ, 859, 33

Goodwin, S. P., Whitworth, A. P., & Ward-Thompson, D. 2004, A&A, 414, 633

Green, J. D., Pontoppidan, K. M., Reiter, M., et al. 2024, ApJ, 972, 5

Greisen, E. W. 2003, in Astrophysics and Space Science Library, Vol. 285, Information Handling in Astronomy - Historical Vistas, ed. A. Heck, 109

Güdel, M. 2002, Annual Review of Astronomy and Astrophysics, 40, 217

Haisch, Karl E., J., Barsony, M., Greene, T. P., & Ressler, M. E. 2002, AJ, 124, 2841

Harvey, P., Merín, B., Huard, T. L., et al. 2007, ApJ, 663, 1149

Hayashi, M., Shibata, K., & Matsumoto, R. 1997, in Astronomical Society of the Pacific Conference Series, Vol. 121, IAU Colloq. 163: Accretion Phenomena and Related Outflows, ed. D. T. Wickramasinghe, G. V. Bicknell, & L. Ferrario, 717

Herbig, G. H. 1960, ApJS, 4, 337

Hillenbrand, L. A. & White, R. J. 2004, ApJ, 604, 741

Hubrig, S., Carroll, T. A., Scholler, M., & Ilyin, I. 2015, MNRAS, 449, L118

Hubrig, S., Schöller, M., & Yudin, R. V. 2004, A&A, 428, L1

Hubrig, S., Stelzer, B., Schöller, M., et al. 2009, A&A, 502, 283

Hughes, V. A. 1988, ApJ, 333, 788

Iglesias, C. A. & Rogers, F. J. 1996, ApJ, 464, 943

Kaas, A. A., Olofsson, G., Bontemps, S., et al. 2004, A&A, 421, 623

Karttunen, H., Kröger, P., Oja, H., Poutanen, M., & Donner, K. J. 2017, Fundamental Astronomy

Kounkel, M., Hartmann, L., Loinard, L., et al. 2017, ApJ, 834, 142

Kratter, K. M., Matzner, C. D., Krumholz, M. R., & Klein, R. I. 2010, ApJ, 708, 1585

Lada, C. J. 1987, in IAU Symposium, Vol. 115, Star Forming Regions, ed. M. Peimbert & J. Jugaku, 1

Lada, C. J. 1991, The Formation of Low Mass Stars: Observations, ed. C. J. Lada & N. D. Kylafis (Springer Netherlands), 329–364

Lada, C. J. & Wilking, B. A. 1984, ApJ, 287, 610

Lee, K. I., Dunham, M. M., Myers, P. C., et al. 2016, ApJ, 820, L2

Lindegren, L., Hernández, J., Bombrun, A., et al. 2018, A&A, 616, A2

Loinard, L., Mioduszewski, A. J., Rodríguez, L. F., et al. 2005, ApJ, 619, L179

Loinard, L., Torres, R. M., Mioduszewski, A. J., & Rodríguez, L. F. 2008, ApJ, 675, L29

Loinard, L., Torres, R. M., Mioduszewski, A. J., et al. 2007, ApJ, 671, 546

Ma, C., Arias, E. F., Eubanks, T. M., et al. 1998, AJ, 116, 516

Manoj, P., Bhatt, H. C., Maheswar, G., & Muneer, S. 2006, ApJ, 653, 657

Markwardt, C. B. 2009, in Astronomical Society of the Pacific Conference Series, Vol. 411, Astronomical Data Analysis Software and Systems XVIII, ed. D. A. Bohlender, D. Durand, & P. Dowler, 251

Menten, K. M., Reid, M. J., Forbrich, J., & Brunthaler, A. 2007, Astronomy and Astrophysics, 474, 515

Mikkola, S. 1987, Celestial Mechanics, 40, 329

Morales-Calderón, M., Stauffer, J. R., Stassun, K. G., et al. 2012, ApJ, 753, 149

Nguyen, C. T., Costa, G., Girardi, L., et al. 2022, A&A, 665, A126

Offner, S. S. R., Kratter, K. M., Matzner, C. D., Krumholz, M. R., & Klein, R. I. 2010, ApJ, 725, 1485

Ordóñez-Toro, J., Dzib, S. A., Loinard, L., et al. 2024, AJ, 167, 108

Ortiz-León, G. N., Dzib, S. A., Kounkel, M. A., et al. 2017a, ApJ, 834, 143

Ortiz-León, G. N., Loinard, L., Dzib, S. A., et al. 2018a, ApJ, 865, 73

Ortiz-León, G. N., Loinard, L., Dzib, S. A., et al. 2018b, ApJ, 869, L33

Ortiz-León, G. N., Loinard, L., Kounkel, M. A., et al. 2017b, ApJ, 834, 141

Padoan, P., Nordlund, Å., Kritsuk, A. G., Norman, M. L., & Li, P. S. 2007, ApJ, 661, 972

Palla, F. & Stahler, S. W. 1993, ApJ, 418, 414

Palla, F. & Stahler, S. W. 1999, ApJ, 525, 772

Parker, E. N. 1955, ApJ, 122, 293

Paxton, B., Bildsten, L., Dotter, A., et al. 2011, ApJS, 192, 3

Pecaut, M. J. & Mamajek, E. E. 2013, ApJS, 208, 9

Perryman, M. 2018, The Exoplanet Handbook

Pietrinferni, A., Cassisi, S., Salaris, M., & Castelli, F. 2004, ApJ, 612, 168

Pietrinferni, A., Cassisi, S., Salaris, M., & Castelli, F. 2006, ApJ, 642, 797

Pontoppidan, K. M., van Dishoeck, E. F., & Dartois, E. 2004, A&A, 426, 925

Potekhin, A. Y. 1999, A&A, 351, 787

Prato, L., Simon, M., Mazeh, T., et al. 2002, ApJ, 569, 863

Preibisch, T. 1999, A&A, 345, 583

Prialnik, D. 2009, An Introduction to the Theory of Stellar Structure and Evolution

Price, D. J. & Bate, M. R. 2007, MNRAS, 377, 77

Raghavan, D., McAlister, H. A., Henry, T. J., et al. 2010, ApJS, 190, 1

Reid, M. J. & Brunthaler, A. 2004, ApJ, 616, 872

Reid, M. J. & Honma, M. 2014, Microarcsecond Radio Astrometry, Vol. 52, 339–372

Richichi, A., Leinert, C., Jameson, R., & Zinnecker, H. 1994, A&A, 287, 145

Rieke, G. H., Rieke, M. J., & Paul, A. E. 1989, ApJ, 336, 752

Rodriguez, L. 1997, in IAU Symposium, Vol. 182, Herbig-Haro Flows and the Birth of Stars; IAU Symposium No. 182, ed. B. Reipurth & C. Bertout

Schleicher, D. R. G., Hidalgo, J. P., & Galli, D. 2023, A&A, 678, A204

Seidelmann, P. K. 1992, Explanatory Supplement to the Astronomical Almanac. A revision to the Explanatory Supplement to the Astronomical Ephemeris and the American Ephemeris and Nautical Almanac.

Shu, F. H., Adams, F. C., & Lizano, S. 1987, ARA&A, 25, 23

Siess, L., Dufour, E., & Forestini, M. 2000, A&A, 358, 593

Skinner, S. L., Güdel, M., Audard, M., & Smith, K. 2004, ApJ, 614, 221

Skinner, S. L. & Yamauchi, S. 1996, ApJ, 471, 987

Spada, F., Demarque, P., Kim, Y. C., Boyajian, T. S., & Brewer, J. M. 2017, ApJ, 838, 161

Stamatellos, D. & Whitworth, A. P. 2009, MNRAS, 392, 413

Stassun, K. G., Feiden, G. A., & Torres, G. 2014, New A Rev., 60, 1

Stelzer, B., Flaccomio, E., Montmerle, T., et al. 2005, ApJS, 160, 557

Stelzer, B., Micela, G., Hamaguchi, K., & Schmitt, J. H. M. M. 2006, A&A, 457, 223

Thompson, A. R., Moran, J. M., & Swenson, George W., J. 2001, Interferometry and Synthesis in Radio Astronomy, 2nd Edition

Tobin, J. J., Looney, L. W., Li, Z.-Y., et al. 2016, ApJ, 818, 73

Tognelli, E., Prada Moroni, P. G., & DeglÍnnocenti, S. 2011, A&A, 533, A109

Tokovinin, A. & Moe, M. 2020, MNRAS, 491, 5158

Tout, C. A. & Pringle, J. E. 1995, MNRAS, 272, 528

Tychoniec, Ł., Hull, C. L. H., Tobin, J. J., & van Dishoeck, E. F. 2018, in IAU Symposium, Vol. 332, Astrochemistry VII: Through the Cosmos from Galaxies to Planets, ed. M. Cunningham, T. Millar, & Y. Aikawa, 249–253

Vousden, W. D., Farr, W. M., & Mandel, I. 2016, MNRAS, 455, 1919

Wade, G. A., Alecian, E., Grunhut, J., et al. 2011, in Astronomical Society of the Pacific Conference Series, Vol. 449, Astronomical Polarimetry 2008: Science from Small to Large Telescopes, ed. P. Bastien, N. Manset, D. P. Clemens, & N. St-Louis, 262

Wade, G. A., Drouin, D., Bagnulo, S., et al. 2005, A&A, 442, L31

Wilking, B. A., Gagné, M., & Allen, L. E. 2008, in Handbook of Star Forming Regions, Volume II, ed. B. Reipurth, Vol. 5, 351

Wilking, B. A., Meyer, M. R., Robinson, J. G., & Greene, T. P. 2005, AJ, 130, 1733

Winston, E., Megeath, S. T., Wolk, S. J., et al. 2007, The Astrophysical Journal, 669, 493

Yi, S., Demarque, P., Kim, Y.-C., et al. 2001, ApJS, 136, 417

Zapata, L. A., Loinard, L., Rodríguez, L. F., et al. 2013, ApJ, 764, L14

Zhao, B. & Li, Z.-Y. 2013, ApJ, 763, 7